Remote Sensing of Environment 316 (2025) 114516

Contents lists available at ScienceDirect

Remote Sensing of Environment

journal homepage: www.elsevier.com/locate/rse

Incorporating environmental stress improves estimation of photosynthesis from NIRvP in US Great Plains pasturelands and Midwest croplands

Lun Gao [a,b,*], Kaiyu Guan [a,b,c,*], Chongya Jiang [a,b], Xiaoman Lu [a,b], Sheng Wang [a,b], Elizabeth A. Ainsworth [a,d,e], Xiaocui Wu [a,b], Min Chen [f]

[a] Agroecosystem Sustainability Center, Institute for Sustainability, Energy, and Environment, University of Illinois Urbana-Champaign, Urbana, IL 61801, USA
[b] Department of Natural Resources and Environmental Sciences, College of Agricultural, Consumers, and Environmental Sciences, University of Illinois Urbana-Champaign, Urbana, IL 61801, USA
[c] National Center for Supercomputing Applications, University of Illinois Urbana-Champaign, Urbana, IL 61801, USA
[d] Department of Plant Biology, University of Illinois Urbana-Champaign, Urbana, IL 61801, USA
[e] USDA-ARS, Global Change and Photosynthesis Research Unit, Urbana, IL 61801, USA
[f] Department of Forest and Wildlife Ecology, University of Wisconsin–Madison, Madison, WI 53706, USA

ARTICLE INFO

Keywords:
Gross primary production
Near-infrared reflectance of vegetation
Light use efficiency
Air temperature
Vapor pressure deficit

ABSTRACT

Near-infrared reflectance of vegetation multiplied by incoming sunlight (NIRvP) is important for gross primary production (GPP) estimation. While NIRvP is a useful indicator of canopy structure and solar radiation, its association with heat or moisture stress is not fully understood. Thus, this research aimed to explore the impact of air temperature (Ta) and vapor pressure deficit (VPD) on the NIRvP-GPP relationship. Using Moderate Resolution Imaging Spectroradiometer (MODIS) observations, eddy-covariance measurements, and the Parameter–Elevation Regressions on Independent Slopes Model (PRISM) data, we found that NIRvP cannot fully explain the response of plant photosynthesis to Ta and VPD at both seasonal and daily scales. Therefore, we incorporated a polynomial function of Ta and an exponential function of VPD to correct its seasonal response to stress and calibrated the GPP residual via a linear function of Ta and VPD time-varying derivatives to account for its daily response to stress. Leave-one-site-out cross-validation suggested that the improvements relative to its original version were especially noteworthy under stress conditions while less significant when there was no water or heat stress across grasslands and croplands. When compared to six other GPP models, the enhanced NIRvP model consistently outperformed them or performed comparably with the best model in terms of bias, RSME, and coefficient of determinant against measurements in grasslands and croplands. Moreover, we found that parameterizing the fraction of photosynthetically active radiation term using NIRv notably improved the performance of the classic MOD17 and vegetation photosynthesis model, with an average RMSE reduction of 13 % across grasslands and croplands. Overall, this study highlights the need to consider environmental stressors for improved NIRvP-based GPP and shed light on future improvements of LUE models.

1. Introduction

Terrestrial gross primary production (GPP) is responsible for the CO_2 uptake of approximately 120–150 Pg C $year^{-1}$, roughly one-sixth of the total atmospheric CO_2 pool (Beer et al., 2010; Anav et al., 2015; Ryu et al., 2019). The carbon fixed through plant photosynthesis provides the material basis for the functioning of life on Earth. Slight perturbations in GPP could remarkably alter the carbon balance of terrestrial ecosystems, nutrient availability, biodiversity, and climate change (Law et al., 2002; Piao et al., 2009; Running, 2012; Ahlström et al., 2015). Thus, accurate quantification of GPP and its variability is crucial in plant biology and global change studies. Originating from trace amounts of energy released during plant photosynthesis, solar-induced chlorophyll fluorescence (SIF) has received increasing attention in GPP estimates since the serendipitous advances in its spaceborne observing capabilities in the early 2010s (Guanter et al., 2007; Frankenberg et al., 2011; Guanter et al., 2012; Joiner et al., 2014; Xiao et al., 2019). Due to SIF's unique mechanistic connection to photosynthesis, it offers a more direct

* Corresponding authors at: Agroecosystem Sustainability Center, Institute for Sustainability, Energy, and Environment, University of Illinois Urbana-Champaign, Urbana, IL 61801, USA.
E-mail addresses: gaoxx996@umn.edu (L. Gao), kaiyug@illinois.edu (K. Guan).

https://doi.org/10.1016/j.rse.2024.114516
Received 5 June 2024; Received in revised form 9 November 2024; Accepted 10 November 2024
Available online 15 November 2024

way to approximate GPP than conventional vegetation indices (Guanter et al., 2014; Yang et al., 2015; Guan et al., 2016; Miao et al., 2018; Mohammed et al., 2019; He et al., 2020; Wu et al., 2022).

While SIF integrates the information of photosynthetically active radiation (PAR), plant structure, and plant physiology to a great extent (Frankenberg and Berry, 2018), spaceborne SIF observations often suffer from low spatiotemporal resolution and substantial spatial gaps (Sun et al., 2023). Although machine learning techniques can partially address this deficiency with the help of additional information (Zhang et al., 2018; Gentine and Alemohammad, 2018; Li and Xiao, 2019), it still notably limits its applications and promotes the research on alternative solutions. Largely inspired by SIF, Badgley et al. (2017) proposed a novel and parsimonious vegetation index for GPP estimation, namely the near-infrared reflectance of vegetation (NIRv) that is the product of the normalized difference vegetation index (NDVI) (Tucker et al., 1985) and NIR. Physically, NIRv explains the fraction of NIR light reflected by vegetation and thus can well approximate the fraction of photosynthetically active radiation (FPAR) absorbed by plants (Badgley et al., 2017). As documented, NIRv demonstrates a superior ability to estimate GPP compared to SIF, without the need for extra auxiliary inputs typically required for traditional vegetation indices-based estimates (Running and Nemani, 1988; Badgley et al., 2019; Zhang et al., 2022). However, unlike SIF observations, NIRv — as a vegetation index — is inherently insufficient to fully capture GPP dynamics under varying environmental stress scenarios due to its lack of consideration of PAR and plant efficiency in using radiation for photosynthesis (Zeng et al., 2019). Specifically, such limitations could make it hard to reflect the rapid GPP change and/or seasonal shifts in GPP influenced by light, heat, or water stress.

So far, great endeavors have been undertaken to enhance NIRv's capacity to accurately quantify GPP variations in response to light and environmental stress. Recently, Dechant et al. (2020, 2022) explored the product of NIRv and PAR (NIRvP) and Wu et al. (2020) investigated the near-infrared radiance of vegetation (NIRvR), both of which showed an improved correlation with GPP across daily to yearly time scales. Meanwhile, Jiang et al. (2021) developed the SatelLite Only Photosynthesis Estimation (SLOPE) model based on the same concept as NIRvP but using a soil-corrected NIRv, which has demonstrated its accurate performance across the continental US when benchmarked against AmeriFlux eddy covariance (EC) data. Their excellence at varying time scales is mainly attributed to the following two aspects. First, NIRv can well capture plant structure changes and partially reflects the impact of environmental stress on plants over monthly/yearly time scales through changes in vegetation structure. Secondly, by adding PAR, not only instantaneous incident solar radiation is accounted for, but also partial environmental heat and water stress, as they have certain correlations (Stearns and Carlson, 1960; Bristow and Campbell, 1984). However, none of these methods can comprehensively explain changes in plant physiological information. Given that plant physiology directly controls how efficiently plants use radiation for photosynthesis and varies promptly with environmental factors, failure to account for it could lead to a significant overestimation of GPP under stress conditions.

Although such a challenge has not been addressed for NIRv, it is worth noting that accounting for environmental stress for GPP estimation has been frequently investigated within the light use efficiency (LUE) model framework. Currently, numerous methods have been proposed to quantify the impact of LUE on GPP through different environmental factors, among which heat and moisture are the most crucial ones (Pei et al., 2022). This is because photosynthetic enzyme activity decreases when air temperature (Ta) deviates from the optimum (Bernacchi et al., 2002; Moore et al., 2021) while increased water stress due to reduced soil moisture (SM) and/or elevated vapor pressure deficit (VPD) hinders uptake of soil water by plant roots and triggers stomatal closure (Novick et al., 2016; Sulman et al., 2016; Liu et al., 2020a; Rigden et al., 2020; Zhang et al., 2021). So far, multiple algorithms have been developed to account for Ta effects, including the min-max scaling function with/without considering optimal Ta (Prince and Goward, 1995; Xiao et al., 2004a; Wang et al., 2015), ramp function (Running et al., 1999; He et al., 2013), exponential function (Wang et al., 2018; Veroustraete et al., 2002), and polynomial function (Cui et al., 2016). On the other hand, parameterizing water stress can be categorized into four groups based on the origin of the stress, including (1) atmospheric water stress based method (Running et al., 1999; Xiao et al., 2004a; Wang et al., 2015; Zhang et al., 2016), (2) soil water stress based method (Landsberg and Waring, 1997), (3) plant water stress based method (Potter et al., 1993; Yuan et al., 2007; Yuan et al., 2010; Gao et al., 2014; Yan et al., 2015; Cui et al., 2016; de Almeida et al., 2018), and (4) combined method (Prince and Goward, 1995; Zhang et al., 2015; He et al., 2016; Wang et al., 2018; Stocker et al., 2019). In addition to heat and moisture stress, some models also consider other factors such as carbon dioxide concentration and freezing conditions, but less frequently (Veroustraete et al., 2002; He et al., 2016).

Considering that Ta and VPD are most frequently used to interpret plant physiological information under heat and water stress (Running et al., 1999; Xiao et al., 2004a; Pei et al., 2022), this study aimed to quantify their impact on the NIRvP-GPP relationship and improve it. Meanwhile, since NIRv has never been examined within the framework of the classic LUE model, such investigations can provide insights into future improvements of LUE models. Specifically, we strive to answer the following questions: (1) How do Ta and VPD impact the relationship between NIRvP and GPP? (2) How can we effectively integrate Ta and VPD with NIRvP for improved GPP estimates? (3) How does the enhanced NIRvP model perform relative to other LUE models, including LRC-NIRvP (Khan et al., 2022), MOD17 (Running et al., 2004; Zhao et al., 2005), MOD17-NIRvP, vegetation photosynthesis model (VPM) (Xiao et al., 2004a; Zhang et al., 2017), VPM-NIRvP, and two-leaf LUE (TL-LUE) model (He et al., 2013; Wu et al., 2015; Zhou et al., 2016)? Here, MOD17-NIRvP and VPM-NIRvP models are variants of MOD17 and VPM models but their FPAR terms are set to be equal to NIRv. To answer these questions, we focused on the SLOPE model and narrowed down the analysis to the US Great Plains pasturelands and Midwest croplands. This is because the US Great Plains pasturelands harbor the majority of the US pasturelands and livestock production (Drummond et al., 2012; USDA NASS, 2018), and the US Midwest produces around $^1/_3$ of the global corn and soybean production (Hatfield, 2012; Heinemann et al., 2014). Additionally, these regions have substantial gradients in both water and heat stress, which provide an important testbed for our proposed methods (Beck et al., 2018).

2. Study area and data

2.1. Study area

Stretching between the Mississippi River and the Rocky Mountains, the Great Plains (Fig. 1) encompasses an expansive elevated plateau characterized by semi-arid grasslands. Elevation varies from 1500 to 1800 m at the foot of the Rockies, gradually descending to ~500 m at the eastern border. The Great Plains experiences a continental climate with distinct seasonal patterns. Throughout most of the region, cold winters and warm summers are prevalent, accompanied by low levels of precipitation and humidity and rapid temperature fluctuations (Beck et al., 2018). Moisture primarily originates from the Gulf of Mexico, resulting in reduced rainfall towards the north and west. Typically, the Great Plains receives more rainfall during the summer than in the winter. Due to its unique geographical features, the Great Plains serves as the primary location for the majority of the US pasturelands and is responsible for approximately 50 % of the total beef cattle herd in the United States (USDA NASS, 2018; Klemm and Briske, 2021).

The U.S. Corn Belt (Fig. 1) occupies the Midwest States of Iowa, Illinois, Indiana, Ohio, Michigan, Wisconsin, and Minnesota, and stretches into the Great Plain States of North Dakota, South Dakota, Nebraska, and Kansas (Green et al., 2018). Most states are lowlands with

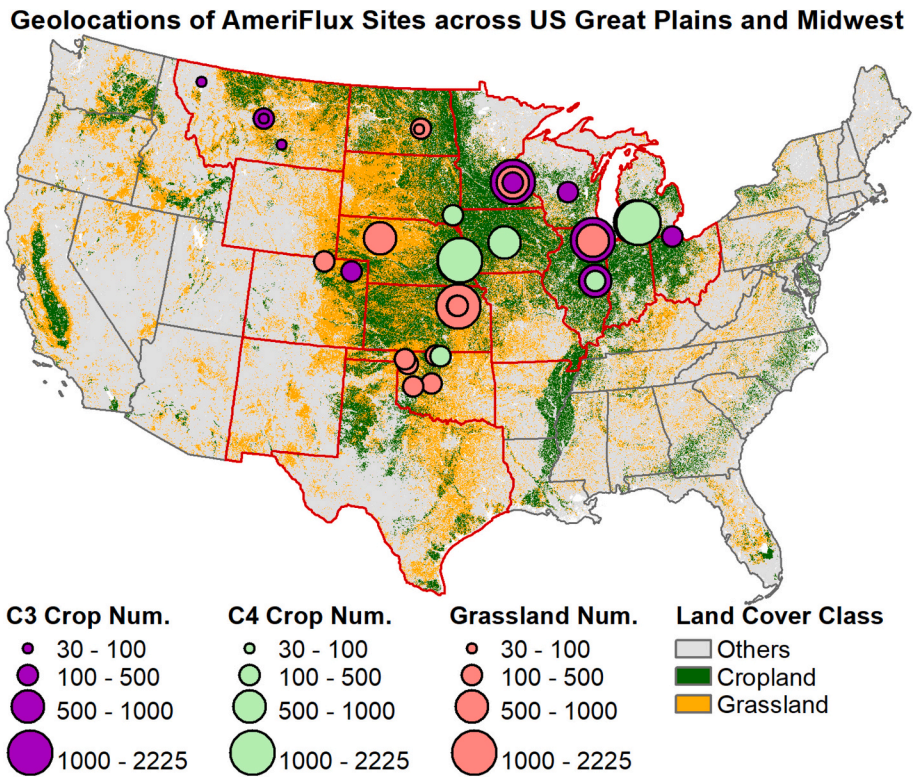

Fig. 1. Study area and geographical locations of 39 AmeriFlux sites throughout the Great Plains grasslands and Midwest croplands of the United States, superimposed on the 30-m land cover map from the National Land Cover Database (NLCD) data in 2019. The state boundaries of the Great Plains and Midwest are highlighted in red. The "Num." in the inset denotes the total number of days of EC observations. (For interpretation of the references to colour in this figure legend, the reader is referred to the web version of this article.)

elevations below 500 m. According to the Köppen-Geiger classification (Beck et al., 2018), the majority of the Midwest experiences a humid continental climate characterized by notable temperature variation between seasons and consistent precipitation throughout the year. The Midwest is one of the world's most productive agricultural regions (Hatfield, 2012). Its fertile soil, relatively flat topography, and plentiful water resources make it particularly suitable for crop cultivation. The combination of a humid climate with warm summers is instrumental in shaping the agricultural landscape of the region, enabling the cultivation of vast corn and soybean fields with minimal irrigation requirements (Green et al., 2018).

2.2. Data for SLOPE model

Following the SLOPE model (Jiang and Guan, 2020, Jiang et al., 2021), this study used soil-adjusted NIRv, PAR, and C4 fraction data at a 250-m spatial grid from 2000 to 2019 (Table 1). Specifically, NIRv was calculated using 250-m MODIS surface reflectance of red and NIR from both MOD09GQ and MYD09GQ products (Vermote and Wolfe, 2015a; Vermote and Wolfe, 2015b). To ensure data quality, only high-quality surface reflectance observations labeled as "corrected product produced at ideal quality all bands" were retained based on the quality control flag. When cloud optical thickness > 0, we further masked out cloud-contaminated values using 1-km MODIS cloud optical thickness data (Baum et al., 2012). Furthermore, to mitigate the impact of the Bidirectional Reflectance Distribution Function (BRDF) (Schaaf et al.,

Table 1
Specifications of data for the implementation of SLOPE, ESLOPE, MOD17, MOD17-NIRvP, VPM, VPM-NIRvP, and TL-LUE models, including soil-adjusted near-infrared reflectance of vegetation (NIRv), photosynthetically active radiation (PAR), C4 fraction (fC4), EC gross primary productivity (GPP), shortwave radiation (SWR), air temperature (Ta), vapor pressure deficit (VPD), leaf area index (LAI), land surface water index (LSWI), enhanced vegetation index (EVI), and plant functional type (PFT).

Variables	Sources	Spatial Res.	Temporal Res.	Time Coverage	Service Models	Reference
NIRv			Daily			
PAR	SLOPE	250 m	Daily	2000–2019	All NIRvP models	Jiang and Guan (2020)
fC4			Annual		SLOPE	
GPP						
SWR	AmeriFlux	–	Daily	2000–2019	All	Baldocchi et al. (2001)
Ta					All except	
VPD	PRISM	4 km	Daily	2000–2019	LRC-NIRvP	Daly et al. (2000)
LAI					MOD17	
	MCD15A3H	500 m	4-day	2000–2019	TL-LUE	Chen and Black (1992)
LSWI					VPM	
	MOD09A1	500 m	8-day	2000–2019	VPM-NIRvP	Vermote (2015)
EVI					VPM	
PFT	MCD12C1	0.05°	Annual	2001–2019	All	Friedl and Sulla-Menashe (2015)

2002) on NIRv, we averaged MOD- and MYD-derived NIRv estimates within a day when their difference was below a threshold of 0.1, considering that the BRDF effect on NIRv at similar solar zenith angles is hardly larger than 0.1. In cases where the absolute difference between MOD- and MYD-derived NIRv exceeded 0.1, we selected the larger value assuming that the smaller value was influenced by clouds. Additionally, assuming there are no extreme events like hailstorms or fire, a temporal filter with a window size of a 7-d radius was applied to fill gaps, remove outliers, enhance NIRv smoothness, and reduce the BRDF effect on the temporal variation of NIRv, considering that (1) vegetation structure typically changes smoothly over a short time window, (2) vegetation structure is hard to promptly respond to environmental stress that typically affects plant photosynthesis through stomatal conductance and photosynthetic enzyme activities (Bernacchi et al., 2002; Novick et al., 2016), and (3) NIRv noise is typically higher than its daily variations due to environmental stress (Jiang and Guan, 2020). More details can be referred to (Jiang et al., 2021). It should be noted that as we checked at two randomly selected EC sites (i.e., US-AR1 and US-IB1), the used NIRv (and its derivative) has higher temporal correlations with EC GPP (and GPP derivative) than BRDF-corrected NIRv from the MCD43C4 product, indicating that smoothing NIRv time series shall not have significant impact on its daily variations with stress.

PAR was calculated by upscaling site-level observations using the ensemble from four machine learning approaches (Jiang et al., 2021), including multivariate adaptive regression splines (MARS) (Friedman, 1991), least absolute shrinkage and selection operator (LASSO) (Tibshirani, 1996), random forest regression (RF) (Liaw and Wiener, 2002), and k-nearest neighbor regression (KNN) (Goldberger et al., 2004). Specifically, ground benchmark data were first computed as the product of the top-of-atmosphere shortwave radiation (SWR_{TOA}), atmospheric transmittance (SWR/SWR_{TOA}), and the ratio of PAR within the shortwave range (PAR/SWR). SWR_{TOA} was determined according to the day of the year (DOY) and latitude (Allen et al., 1998) while the calculation of daily mean SWR and PAR was based on ground observations from seven long-term continuous sites across the Surface Radiation Budget (SURFRAD) network (Augustine et al., 2000) with an interval of less than 3 min between 2000 and 2018. To impose more physical constraints on the machine-learning PAR calculation, multiple satellite-based forcing datasets were obtained from MODIS Terra and Aqua observations, including 3-km aerosol optical depth (MOD04_3K and MYD04_3K) (Remer et al., 2013), 1-km total column water vapor (MOD05_L2 and MYD05_L2) (Chang et al., 2014), 1-km cloud optical thickness (MOD06_L2 and MYD06_L2) (Baum et al., 2012), 5-km total column ozone burden (MOD07_L2 and MYD07_L2) (Seemann et al., 2006), and 500-m white-sky land surface shortwave albedo (MCD43A3) (Román et al., 2009). In addition, 30-m altitude data were also collected from the Shuttle Radar Topography Mission Global 1 Arc Second mission (Kobrick and Crippen, 2013). All machine learning approaches were trained and validated through the 5-fold cross-validation based on available data. It should be noted that to circumvent the influence of uncertainties in machine learning derived PAR on the analysis, we also calculated PAR based on the shortwave radiation measurements from AmeriFlux sites for all site-level analyses by multiplying a constant value that was calibrated against machine learning-derived PAR.

To investigate the impact of heat and water stress on the SLOPE model, we conducted analyses using daily 4-km Ta and VPD data obtained from the Parameter–Elevation Regressions on Independent Slopes Model (PRISM) (Daly et al., 2000; Johnson et al., 2000). Developed by the PRISM Climate Group at Oregon State University (Daly et al., 2008), PRISM was originally designed to map precipitation, which was further expanded to monitor Ta and dew point along with other climate variables. Considering the marked correlation between elevation and climate, PRISM generates the gridded climate variables using a climate-elevation regression weighted by station observation data and other physiographic factors such as topographic position and vertical atmospheric layer. In this study, we performed the analysis using both daily average and maximum values for Ta and VPD. Analysis of average and maximum values was incorporated because maximum and minimum temperatures can exhibit significant day-to-day variation, whereas minimum VPD tends to remain relatively constant (Fig. A1 in the Appendix). The daily mean Ta and VPD were computed by averaging daily minimum and maximum values. We note that the PRISM data were used rather than the downscaled ERA-Interim reanalysis data (Dee et al., 2011) since the PRISM dataset has higher spatial resolution than ERA-Interim reanalysis data and can be directly used to produce the regional GPP map. Moreover, these two datasets are highly correlated with each other across studied AmeriFlux sites, as we examined in Fig. A1 in the Appendix.

2.3. Data for other models

To evaluate the performance of the enhanced SLOPE (ESLOPE) model, we compared it with other models, including LRC-NIRvP, MOD17, MOD17-NIRvP, VPM, VPM-NIRvP, and TL-LUE models. To keep the comparison fair during the leave-one-site-out cross-validation process, we directly implemented these models rather than using their official products (if they existed) and used the same suite of Ta and VPD from the PRISM to parameterize water and heat stress when needed. For the implementation of the MOD17 and MOD17-NIRvP models, we used the 500-m 4-day composite leaf area index (LAI) from MODIS (MCD15A3H, Version 6.1) (Chen and Black, 1992) instead of the LAI climatology used by official products. The 4-day LAI composite was temporally interpolated into a daily time scale using the linear interpolation method. On the other hand, when implementing the VPM and VPM-NIRvP models, we computed the enhanced vegetation index (EVI) (Huete et al., 1997) and land surface water index (LSWI) (Xiao et al., 2004a) using MODIS surface reflectance of red, NIR, blue, and shortwave infrared from the MOD09A1 (version 6) product (Vermote, 2015). This product is a composite of 8-day observations from the Terra satellite at a 500-m spatial resolution and was temporally interpolated into a daily time scale using the linear interpolation method. Note that the self-implemented MOD17 and VPM models should have better or at least comparable performance to their official counterparts considering that their maximum LUE values are calibrated against local EC measurements in this study.

2.4. Eddy covariance GPP

The calibration and validation of SLOPE and ESLOPE GPP were performed using the observations obtained from AmeriFlux sites, which employed the nighttime partitioning method to partition the net ecosystem CO_2 exchange into GPP and respiration (Baldocchi et al., 2001; Reichstein et al., 2005; Wutzler et al., 2018). Specifically, we initially collected the measurements from 176 sites with 3520 site years across the US Great Plains and Corn Belt from 2000 to 2019, which includes all FLUXNET2015 Tier 1 data (Pastorello et al., 2020) that were generated through a standardized data processing pipeline. For sites not included in FLUXNET2015 Tier 1 data, we employed the Open Network-Enabled Flux processing pipeline (ONEFlux) (Pastorello, 2019) to gap-fill meteorological and flux measurements and partition CO_2 fluxes into respiration and photosynthesis components. To control the quality of daily average GPP (i.e., GPP_DT_VUT_MEAN), we masked out all values when the quality flag (i.e., NEE_VUT_REF_QC) was below 0.8. Besides, we confined our analysis to the sites where the coefficient of determination between NIRv and measured GPP was more than 0.5 to further mitigate the spatial representativeness issue of EC measurements due to heterogeneous vegetation, wind directions, atmospheric turbulent states, and measurement height (Barcza et al., 2009; Chen et al., 2012). The threshold of 0.5 was determined based on the facts that NIRv has a moderate to high correlation with GPP (Badgley et al., 2017). Moreover, we further evaluated the spatial representativeness of selected EC sites using the 30-m Cropland Data Layer (CDL) (Boryan

et al., 2011) within 250-m radial distance from the tower from 2008 to 2019 (Chu et al., 2021), which indicated that most sites had moderate to high spatial representativeness with dominant land cover exceeding 50 % (Fig. A2 in the Appendix). In addition, sites with less than 30 days of observations were excluded, resulting in a final selection of 16 sites (73 site years) in grasslands, 15 sites (91 site years) in C4 croplands, and 17 sites (61 site years) in C3 croplands for analysis. The distribution of these sites is depicted in Fig. 1.

2.5. Land cover

The annual 250-m C4 fraction data were calculated based on the National Land Cover Database (NLCD) (Homer et al., 2004) and Cropland Data Layer (CDL) (Boryan et al., 2011). Produced by the United States Geological Survey (USGS), NLCD provides a high-quality land cover classification at a spatial resolution of 30 m (Fig. 1), which has been updated every two to three years starting from 2001. NLCD classes include agriculture, grassland, forest, and urban areas. By contrast, the agriculture-oriented CDL product from the United States Department of Agriculture (USDA) National Agricultural Statistics Service (NASS) offers annual crop cover of more than 100 crop types at a spatial resolution of 30 m starting in 2008. To compute the C4 fraction within the MODIS footprint of 250 m, the fraction of vegetated area was first determined based on NLCD data. Then, the C4 fraction of crops was calculated as the ratio of the C4 fraction in the whole footprint to the fraction of vegetated areas (Jiang et al., 2021). The calculated C4 fraction was then utilized, along with yearly plant functional types (PFTs) from MCD12C1 (Friedl and Sulla-Menashe, 2015) at a spatial resolution of 0.05°, to differentiate between grass, C4 crops, and C3 crops. The determination of the C4 fraction was limited to croplands due to the unavailability of more detailed functional types for grasslands.

3. Methodology

3.1. SLOPE and ESLOPE models

The SLOPE model (Jiang et al., 2021) is derived as follows:

$$GPP = PAR \bullet FPAR \bullet LUE \approx \alpha \bullet NIRvP \tag{1a}$$

$$NIRvP = PAR \bullet NIRv \tag{1b}$$

where the constant value α [gC J^{-1}] is calibrated against EC measurements for a specific PFT. *NIRv* denotes soil-corrected NIRv, which is normalized by multi-year climatological maximum and soil background NIRv. The reason why NIRv is further corrected for soil background is that bare-soil NIRv is rarely equal to zero and thus could decay NIRv signals from vegetation, which is analogous to the correction of soil-background effects on EVI for the classic VPM model (Wu et al., 2018). The soil background NIRv values were determined based on the following steps (Jiang et al., 2021). First, for non-forested areas, soil-background NIRv was identified as the lowest value based on the multi-year time series of NIRv. Second, when soil-background NIRv was greater than 0.2, we forced it to 0.2 because soil NDVI is typically less than 0.2 (Montandon and Small, 2008), which was also supported by our hyperspectral reflectance simulation results (Jiang and Fang, 2019). Third, for forested areas that are not considered in this work, it is not necessary to conduct any soil background correction since soils cannot be observed from space. We note that in most cases where bare-soil NIRv is smaller than vegetation-contributed NIRv, the correction of bare-soil NIRv shall not affect the continuity of NIRv. However, the continuity of NIRv will be affected in the presence of bare soils, which is especially important for harvested agricultural fields. In addition, considering that the GPP-NIRv relationship varies significantly across C3 and C4 species (Badgley et al., 2019; Wu et al., 2020), the model further accounts for the area fraction of C4 (f_{C4}) vs C3 for croplands:

$$GPP = \left[\alpha_{C3} \bullet \left(1 - f_{C4}\right) + \alpha_{C4} \bullet f_{C4}\right] \bullet NIRvP \tag{1c}$$

where α_{C3} and α_{C4} are coefficients for C3 and C4 species.

To account for Ta and VPD effects on SLOPE GPP, this study calibrated both SLOPE coefficient α and GPP residuals. Based on our analysis (Section 4.1), Ta effects were parameterized by a quadratic function while VPD effects were calibrated by an exponential decay function (Eq. (2b)). The quadratic function of Ta was considered since it can simulate LUE increase with Ta below an optimum and LUE decrease with Ta above an optimum. In this quadratic polynomial function of Ta, there is no constant term, and thus GPP is 0 gC m^{-2} day^{-1} when Ta is below 0 °C, which is consistent with other classic LUE models (Running et al., 1999; Xiao et al., 2004a). For the exponential decay function of VPD, only one unknown parameter was considered. However, we note that more complex exponential functions might enhance the fitting accuracy during calibration, but they could also introduce greater vulnerability and reduce the robustness of the model. On the other hand, on a daily time scale, we observed a strong correlation between the time-varying derivative difference between SLOPE and EC GPP and the derivatives of daily maximum Ta and VPD. This difference was calibrated using a multivariate linear function of daily maximum Ta and VPD time-varying derivatives (Eq. (2c)). Since the time-varying derivative of GPP only modifies daily variation in GPP, it is expected that this residual term will not significantly affect the seasonal trend of GPP. However, considering that such calibration may render the intercept not equal to 0, we only applied it to high biomass conditions with NIRv greater than 0.1. Finally, the ESLOPE GPP is expressed as follows:

$$GPP = f_1(Ta_{mean}, VPD_{mean}) \bullet NIRvP - f_2(Ta_{max}, VPD_{max}) \tag{2a}$$

$$f_1(Ta_{mean}, VPD_{mean}) = \left(\beta_1 \bullet {Ta_{mean}}^2 + \beta_2 \bullet Ta_{mean}\right) \bullet exp(\beta_3 \bullet VPD_{mean}) \tag{2b}$$

$$f_2(Ta_{max}, VPD_{max}) = \beta_4 \bullet \delta Ta_{max} + \beta_5 \bullet \delta VPD_{max} \tag{2c}$$

where β_i $(i = 1, 2, 3, 4, 5)$ are coefficients fitted based on EC measurements and their values are shown in Table 2. The subscripts of 'mean' and 'max' denote daily mean and maximum values.

3.2. Other GPP models for comparison

To comprehensively evaluate the performance of the proposed model, we compared it with other six GPP models, including NIRvP based light response curve model (LRC-NIRvP) (Khan et al., 2022), MOD17 model (Running et al., 1999), NIRvP based MOD17 model (MOD17-NIRvP), VPM (Xiao et al., 2004a; Xiao et al., 2004b), NIRvP based VPM (VPM-NIRvP), and two-leaf LUE model (TL-LUE) (He et al., 2013; Wu et al., 2015; Zhou et al., 2016). MOD17-NIRvP and VPM-NIRvP models are directly adapted from the MOD17 and VPM but their FPAR terms are set to be equal to NIRv, which can help evaluate the performance of the developed stress calibration methods relative to existing classical approaches. Note that despite the difference in magnitude between FPAR and NIRv, this difference can be eliminated using the calibrated coefficient in Eq. (2b), given that NIRv has a significant linear correlation with MOD17/VPM FPAR, which was examined using all available data across EC sites (not shown here). More details about the model and parameterizations are provided in Appendix C.

Table 2
Values of β_i $(i = 1, 2, 3, 4, 5)$ used in Eq. (2).

PFT	β_1	β_2	β_3	β_4	β_5
Grassland	−0.0039	0.2677	−0.0149	0.1236	−0.0379
C3 Cropland	−0.0031	0.2223	−0.0033	0.1275	0.0532
C4 Cropland	−0.0036	0.2873	−0.0007	0.2006	0.0436

3.3. Data analysis and performance evaluation

To study how SLOPE GPP responded to Ta and VPD, we focused the analysis on the peak growing season from June to September to be consistent with previous works (Fu et al., 2020; Liu et al., 2020a, 2020b; He et al., 2021; Wang et al., 2022; Gao et al., 2024). This is not only because vegetation in off-peak growing season is very sparse in US Great Plains pasturelands and Midwest croplands, but also because moisture and heat predominantly control ecosystem fluxes during the peak growing season (Liu et al., 2020a, 2020b; He et al., 2021; Wang et al., 2022), which could facilitate answering our first scientific question about how do Ta and VPD impact the relationship between NIRvP and GPP. Besides, we note that while NIRv may reach saturation in densely vegetated areas during the peak growing season due to the saturation problem of NDVI (Huete et al., 2002), it was documented that NIRv is less likely to saturate than traditional vegetation indices (Baldocchi et al., 2020; Mengistu et al., 2021). Moreover, as we examined per EC site, NIRv saturation was not found in US Great Plains pasturelands and Midwest croplands.

In addition, we performed analyses on both daily and seasonal time scales. On a seasonal scale, we used a statistical data binning analysis (Liu et al., 2020a; Zhou et al., 2019; Gao et al., 2024) for the parameter α in Eq. (1a) with respect to Ta and VPD. Specifically, for different plant functional types (PFTs), we calculated α values at different levels of Ta or VPD to check whether α varied or not, where Ta and VPD were binned using a sliding window of 2 °C and 2 hPa around their center. To detect the daily-scale impacts of Ta and VPD on SLOPE GPP, we computed the time-varying derivatives of GPP, Ta, and VPD, which is the difference between values on two consecutive days. Then, the correlation between the time-varying derivative of Ta/VPD and the difference between SLOPE and AmeriFlux EC GPP time-varying derivatives (δGPP_S - δGPP_A) was used as a metric to measure the coupling between SLOPE GPP, Ta, and VPD at a daily time scale. This is because EC GPP captures the daily-scale effects of Ta and VPD, and thus any deviations between SLOPE and EC GPP time-varying derivatives are likely caused by inaccurate representation of Ta and VPD in SLOPE. These analyses were further used to guide the calibration of Ta and VPD effects on the SLOPE model, leading to the development of the ESLOPE model.

To evaluate the performance of the ESLOPE model, we first comprehensively compared the SLOPE and ESLOPE model. Specifically, we studied the degree to which calibrating SLOPE coefficients and residual can reduce the impacts of Ta and VPD on GPP through the correlation between the SLOPE residual and Ta/VPD. Further, we conducted the leave-one-site-out cross-validation to compare two models along different gradients of Ta and VPD, which can help to check in which cases the improvements are more notable. Note that the leave-one-site-out cross-validation has been frequently used by previous works to improve and validate GPP models (Verma et al., 2014; Verma et al., 2015; Virkkala et al., 2021). Moreover, we examined the time series of SLOPE and ESLOPE GPP to understand how accounting for Ta and VPD contributes to the improvement of the ESLOPE model relative to the SLOPE model. Besides, we checked the difference between spatial patterns of SLOPE and ESLOPE GPP across US Great Plains grasslands and Midwest croplands. On the other hand, we intercompared the ESLOPE model with the SLOPE and six other models by examining diverse error metrics of bias, root-mean-squared error (RMSE), and coefficient of determinant (R^2), which are defined as follows:

$$bias = \mathrm{E}(\widehat{\theta} - \theta)$$

$$RMSE = \sqrt{\mathrm{E}\left[(\widehat{\theta} - \theta)^2\right]}$$

$$R^2 = \frac{(\mathrm{E}[(\widehat{\theta} - \mathrm{E}(\widehat{\theta}))(\theta - \mathrm{E}(\theta))])^2}{\left(\mathrm{E}(\widehat{\theta}^2) - (\mathrm{E}(\widehat{\theta}))^2\right)\left(\mathrm{E}(\theta^2) - (\mathrm{E}(\theta))^2\right)}$$

where E is the expectation, $\widehat{\theta}$ is the estimated parameter, and θ is the measurement. To examine whether the differences among models are significant or not, we resorted to the one-way analysis of variance (ANOVA) (Bewick et al., 2004).

4. Results

4.1. Quantification of Ta and VPD impacts on SLOPE GPP

Fig. 2 presents the SLOPE coefficients calculated using all available site-level data binned by daily mean Ta or VPD across different PFTs. The results highlight the substantial impact of Ta and VPD on SLOPE coefficients and the NIRvP-GPP relationship. Specifically, the SLOPE coefficients increased with daily mean Ta for C3 and C4 crops. As Ta enhanced from 10 to 30 °C, the coefficient increased by 52 % and 116 % for C3 and C4 crops, respectively, resulting in a substantial deviation from the constant coefficient previously used in the SLOPE model. To that end, using a constant coefficient without accounting for Ta effects could lead to a notable overestimation of GPP when Ta is below 15 °C, especially during early and late growing seasons (Fig. A1 in the Appendix) and a marginal underestimation when Ta exceeds 25 °C. However, for grasslands, the binned coefficients did not significantly vary with daily mean Ta, potentially because grasslands represent a diversity of C3 and C4 species with different Ta responses. On the other hand, the SLOPE coefficients decreased by more than 22 % for all three PFTs as VPD increased from 0 to 20 hPa. When compared with the constant SLOPE coefficient, the deviation primarily occurred when VPD was below 5 hPa, which could lead to an underestimation of GPP when a constant coefficient is employed.

Given that the daily mean Ta and VPD contain information pertaining to both high and low temperatures and/or VPD, we also investigated the SLOPE coefficient variation against daily maximum Ta and VPD, as depicted in Fig. D1 in the Appendix. Generally, the results affirmed that the SLOPE coefficient tended to increase with enhanced Ta for C3 and C4 croplands and decrease when VPD increased across all PFTs, especially when the daily maximum Ta and VPD were not at low levels. Nonetheless, when the daily maximum Ta fell below 15 °C or when the daily maximum VPD approached 0 hPa, the SLOPE coefficient showed remarkable fluctuations and did not follow the same trend as observed in Fig. 2. This phenomenon could be attributed to the fact that daily maximum Ta and VPD played a more important role in determining GPP variation when Ta and VPD were relatively high. Therefore, we parameterized the SLOPE coefficient using daily mean values of Ta and VPD for the improved SLOPE GPP estimation.

We also calculated the SLOPE coefficient by grouping data based on both daily mean Ta and VPD, and compared it with the numerical approximations using Eq. (2b). To ensure statistical robustness, bins with sample sizes less than 10 days were discarded. Consistent with Fig. 2, Fig. 3 showed an upward trend in the SLOPE coefficient as Ta increased for croplands and a downward trend in the SLOPE coefficient as VPD increased across all PFTs. Such a trend with Ta and VPD resulted in substantial variation of more than 400 % between the minimum and maximum coefficient values for all three PFTs. To account for the Ta and VPD effects on the SLOPE coefficient, we applied a correction using a polynomial function for Ta and an exponential decay function for VPD (Eq. (2b)). The numerical approximation in Fig. 3 illustrated that the proposed method captured the overall trend of the coefficients with Ta and VPD. Specifically, for all three PFTs, lower values were observed under extremely low Ta and VPD conditions, while higher values were evident when Ta was high and VPD was low. Compared to the binning analysis, the coefficients obtained with the numerical approximation showed smoother transitions along the gradients of Ta and VPD. One notable difference between the binned and approximated SLOPE coefficients occurred when VPD was lower than 10 hPa, with the binned coefficient showing a notably higher value compared to the

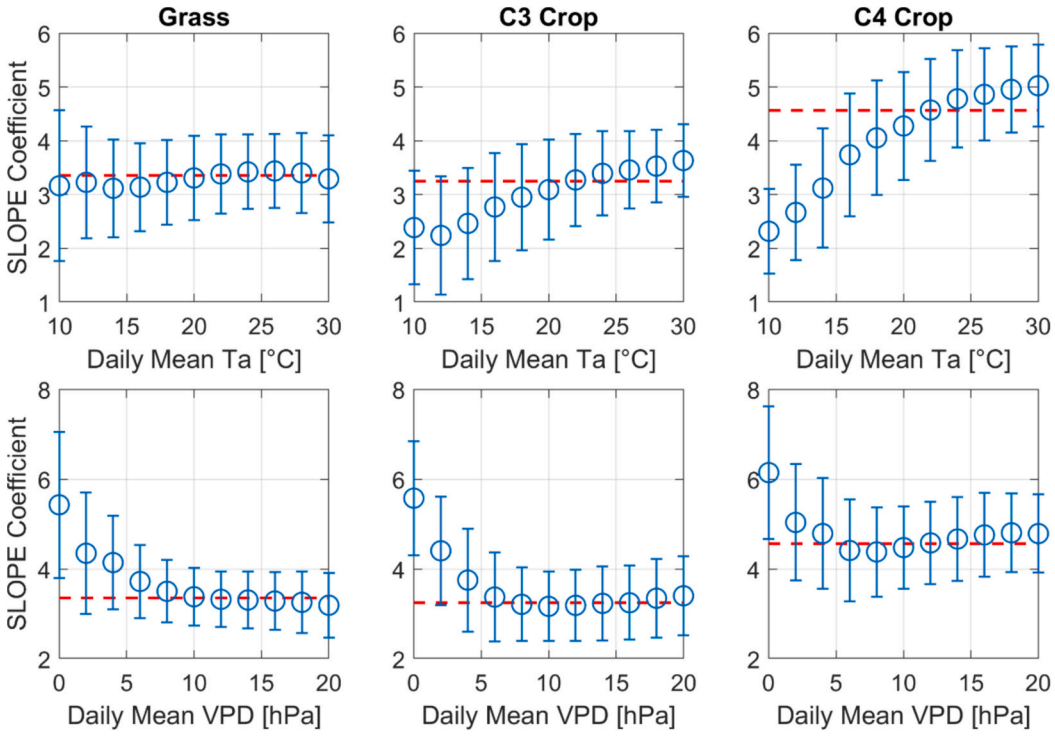

Fig. 2. SLOPE coefficients [gC J^{-1}] binned by daily mean Ta and VPD across US grasslands, C3 and C4 croplands, where the bar length denotes the corresponding standard derivation of all site-level values at each bin. The red dashed line indicates the constant coefficient used by SLOPE. (For interpretation of the references to colour in this figure legend, the reader is referred to the web version of this article.)

approximated values. This is mainly because the exponential decay function of VPD does not have an intercept term. On the other hand, we computed the difference between the SLOPE constant coefficient and binned/approximated coefficients. Significant differences primarily occurred in regions with relatively low data density, characterized by low Ta or high VPD, according to both binning analysis and numerical approximation results. By contrast, in regions where data density exceeded 0.7, the disparity was trivial. This generally aligns with our expectations since the SLOPE constant coefficient was determined by fitting all available data, which could lead to a more substantial difference between the constant coefficient and binned coefficients over regions with lower data density.

In addition, we investigated the immediate impacts of Ta and VPD on SLOPE GPP on a daily time scale by assessing the relationship between δGPP_S - δGPP_A and the corresponding derivatives of daily maximum Ta and VPD. As shown in Fig. 4, there was moderate correlation between daily maximum Ta derivatives and δGPP_S - δGPP_A, with Pearson correlation coefficient $r > 0.2$ for all three PFTs. By contrast, we found more significant correlations between daily maximum VPD derivatives and δGPP_S - δGPP_A with $r > 0.36$ across different PFTs. These results indicate that VPD had a greater influence than Ta in regulating the day-to-day variation of GPP, which is likely due to its direct control over stomatal conductance, as described by Farquhar and Von Caemmerer (1982) and Leuning (1995). On the other hand, we also investigated correlations using daily mean Ta and VPD derivatives, as shown in Fig. D2 in the Appendix. The results were generally consistent with Fig. 4, indicating a notable correlation between δGPP_S - δGPP_A and the daily mean Ta and VPD derivatives. Specifically, the correlation between δGPP_S - δGPP_A and daily mean Ta derivatives was notably lower than that using daily maximum Ta derivatives while the correlation between δGPP_S - δGPP_A and daily mean VPD derivatives was similar to that using daily maximum VPD derivatives. This is not surprising given that both minimum and maximum Ta values vary notably, while the minimum VPD value is relatively constant. Therefore, maximum VPD was probably the major driver of both mean and maximum VPD. Overall, these results suggested accounting for the daily-scale impacts of environmental factors, especially VPD, could improve the SLOPE model.

4.2. Comparison between ESLOPE and SLOPE models

Fig. 5 examines the effects of coefficient and residual calibration on the SLOPE model over C4 croplands, whereas outcomes pertaining to grasslands and C3 croplands can be found in Appendix E. When there is a strong relationship between Ta or VPD and the GPP residuals, performing a direct calibration of the SLOPE coefficient can effectively diminish the dependence of GPP residuals on Ta or VPD. Specifically, compared to the SLOPE model, the significant association between GPP residual and Ta can be reduced by 89 % after the calibration of the SLOPE coefficient (Fig. 5A). Considering that the GPP residual mainly arises from the seasonal and interannual deviation from measurements, these results indicate that calibrating the SLOPE coefficient can effectively improve the SLOPE GPP seasonal and interannual variability with environmental variables. By contrast, such calibration had no effects on the correlation between δGPP_S - δGPP_A and Ta/VPD derivatives (Fig. 5B).

On the other hand, the calibration of the SLOPE residual considerably decreased the dependence of δGPP_S - δGPP_A on Ta/VPD derivatives (Fig. 5B) while having no effects on the association between GPP residual and Ta/VPD (Fig. 5A). As shown, the correlation between δGPP_S - δGPP_A and the derivatives of Ta and VPD was reduced by more than 42 % in comparison with the original SLOPE model; however, the correlation between GPP residual and Ta/VPD remains at the same level. This is generally in line with our expectations since the GPP time-varying derivative mainly depends on its daily rather than seasonal/interannual variation. As a result, the combined calibration of both SLOPE coefficient and derivative residual complements each other, resulting in simultaneous improvements in both seasonal and daily variation of GPP with respect to Ta and VPD. Specifically, the absolute correlation coefficient values between GPP residual and environmental stress and between δGPP_S - δGPP_A and the derivatives of Ta/VPD are all well

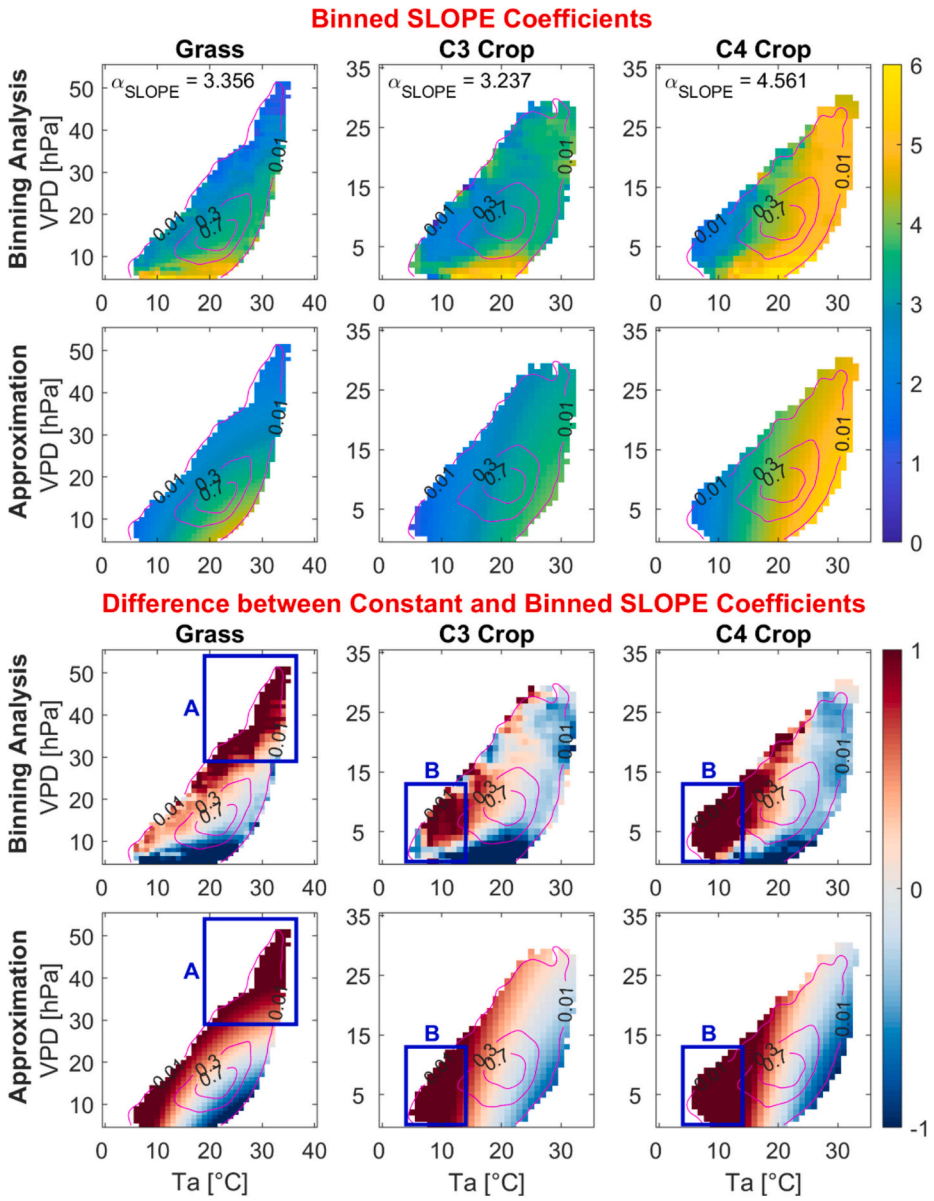

Fig. 3. SLOPE coefficient [gC J^{-1}] as a function of Ta and VPD across grassland, C3 and C4 croplands using both binning analysis and numerical approximation. The binning analysis was performed by grouping data using a Ta threshold of 2 °C and a VPD threshold 2 hPa, while numerical approximation was based on Eq. (2b). The contours and the surrounding numbers depict the data density. Note that the analysis was only conducted for the bins with more than 10-day observations. The constant coefficient used by SLOPE for each land cover was reported in the inset of the first row.

controlled below 0.12. Similar results for grassland and C3 croplands can also be found in Figs. E1 & E2 in the Appendix.

To evaluate the extent of improvement in GPP estimates achieved by ESLOPE as compared to the SLOPE model, we conducted leave-one-site-out cross-validation across different levels of Ta and VPD, including extreme cases, for three distinct PFTs based on data from available AmeriFlux sites. Fig. 6 demonstrates pronounced improvements in GPP accuracy using the ESLOPE model relative to the SLOPE model under extreme Ta and VPD conditions. In the case of grassland, our observations revealed a notable reduction in RMSE when using the ESLOPE model across most Ta and VPD levels relative to the SLOPE model. As checked by the ANOVA test, the extent of RMSE reduction became more significant under stress conditions when Ta fell below 15 °C or exceeded 30 °C or when VPD was greater than 30 hPa. On average, the RMSE decreased by over 10 % across all Ta/VPD levels, but it exhibited a reduction of more than 16 % when VPD exceeded 30 hPa. For C3 croplands, the results illustrate that the ESLOPE model is superior to the SLOPE model at most levels of Ta and VPD. In particular, the reduction in RMSE became more prominent as Ta decreased, leading to a 21 % decrease in RMSE when Ta was less than 15 °C. Note that we also observed a degradation in the performance of ESLOPE GPP relative to SLOPE GPP when Ta was above 25 °C, which may be due to the noise in Ta and NIRv data. By contrast, there were no notable trends between the difference in RMSE of SLOPE and ESLOPE GPP with VPD. Regarding C4 croplands, the ESLOPE model typically performed better than the SLOPE model at most Ta/VPD levels, with the greatest RMSE reduction in low Ta conditions. The RMSE was reduced by more than 40 % when Ta was below 15 °C. Further results in Figs. F1 & F2 in the Appendix demonstrate that the reduction of RMSE along Ta and VPD gradients mainly resulted from the decrease in bias, although the temporal correlation between ESLOPE and measurements was slightly improved across most Ta and VPD gradients. This appeared to align with the difference between the constant and binned coefficients depicted in Fig. 3, suggesting that the incorporation of Ta and VPD into the SLOPE model can overall

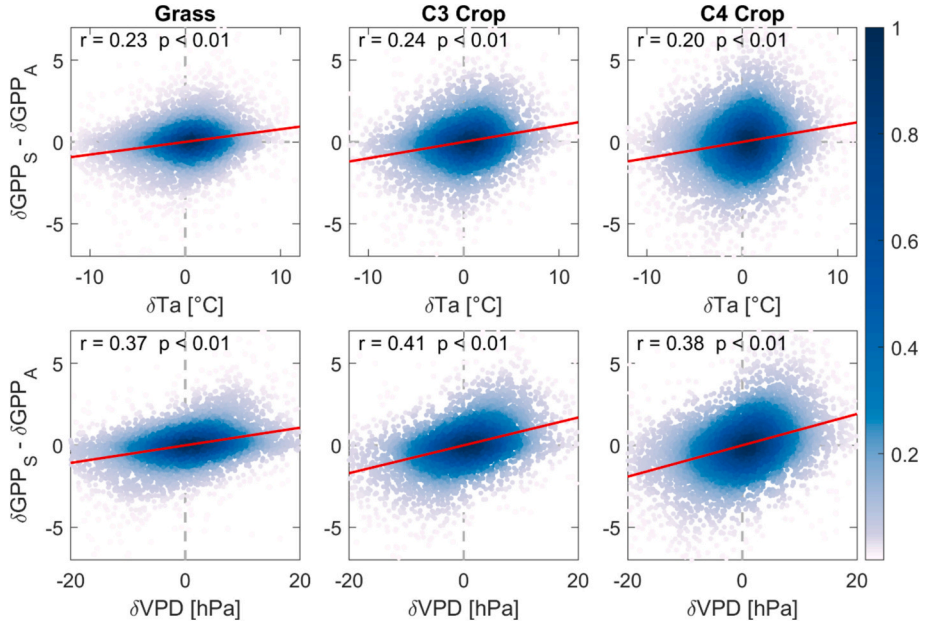

Fig. 4. Relationship between the time-varying derivatives of daily maximum Ta (δTa) and VPD (δVPD) and the differences in time-varying derivatives of SLOPE (δGPP_S) and AmeriFlux GPP (δGPP_A) [gC m^{-2} d^{-1}]. The red line indicates the best-fit linear regression line. (For interpretation of the references to colour in this figure legend, the reader is referred to the web version of this article.)

result in enhanced GPP estimates.

To investigate the circumstances under which accounting for the environmental variables of Ta and VPD can further improve the SLOPE model, here we plotted the GPP time-series estimates from SLOPE and ESLOPE models along with Ta and VPD data during the peak growing season of the C4 crop in 2016 at the US-A74 site (36.8°, −97.5°) (Fig. 7). The reason for selecting the site was due to its exposure to high Ta and VPD with large fluctuations during the study period. The results demonstrate that both ESLOPE and SLOPE estimates could effectively capture the overall seasonal dynamics of GPP measurements, with the coefficient of determinant greater than 0.8. Compared to the SLOPE model, the ESLOPE model notably improved the estimate of GPP when validated against measurements, with a 2.4 % increase in the coefficient of determination and a 3.5 % reduction in RMSE. As indicated by the ANOVA test, the reduction in bias becomes significant ($p < 0.01$) during the period from 06/16/2016 and 07/19/2016 (Fig. 7, light gray part), where Ta is at a notable high level while VPD fluctuates greatly. Consequently, combining Ta and VPD with NIRvP induced a considerable enhancement in the ESLOPE coefficient, which further minimizes the discrepancy between the estimated GPP and measurements. In addition, we also checked the GPP time series at grassland and C3 cropland sites (G1Figs. G1 & G2), showing that accounting for Ta and VPD can notably improve SLOPE GPP estimates when GPP has great daily variability with Ta and VPD.

Furthermore, we implemented the SLOPE and ESLOPE models across US Great Plains grasslands and Midwest croplands during the period from 2000 to 2019 to investigate their differences under the extreme Ta or VPD scenarios. In Fig. 8, we presented the temporally averaged GPP derived from the SLOPE and ESLOPE models as well as their disparity when VPD exceeded 30 hPa or Ta fell below 15 °C, denoted as highlighted Regions A and B in Fig. 3. The results reveal that SLOPE and ESLOPE GPP display similar spatial patterns in both grasslands and croplands but with notable variation in magnitude. Specifically, in the case of high VPD in grasslands, both models consistently indicate an increasing GPP gradient along the longitudinal direction of the US Great Plains, which is aligned with the east-west precipitation gradient (Corbosiero et al., 2009). Using the ANOVA test, we found that ESLOPE GPP is significantly lower than SLOPE GPP, particularly in the eastern Great Plains, where the disparity can be as large as 2 gC m^{-2} d^{-1}. The longitudinal discrepancy could be attributed to the uneven distribution of grass, with sparse vegetation in the midwest Great Plains compared to the eastern region, where the difference between SLOPE and ESLOPE GPP is linked to GPP magnitude. On the other hand, in the low Ta case for croplands, SLOPE GPP is higher than ESLOPE GPP, with the overestimation in SLOPE GPP surpassing 1 gC m^{-2} d^{-1} in the majority of cropland areas. Overall, these results are in line with the binning analysis in Fig. 3, supporting the argument that incorporating environmental variables into the ESLOPE model helps alleviate the overestimation of GPP under extreme Ta and VPD conditions.

4.3. Comparison among different GPP models

In addition, we compared the performance of ESLOPE with SLOPE, LRC-NIRvP, MOD17, MOD17-NIRvP, VPM, VPM-NIRvP, and TL-LUE models through the level-one-site-out cross-validation across grassland, C3 and C4 croplands. The results in Fig. 9 demonstrate that the ESLOPE model typically outperforms most other models across all three PFTs, in terms of bias, RMSE and coefficient of determinant. Regarding bias, the median bias of all models generally remains below 1 gC m^{-2} d^{-1} while no specific model significantly outperforms others in all three PFTs according to the ANOVA test. However, we found that the variances of ESLOPE GPP bias remained stable at a low level in all three PFTs while variances of other models increased notably in the C4 cropland. Concerning RMSE and coefficient of determinant, despite no significant differences being detected between the ESLOPE model and most other models, it was observed that the ESLOPE model was generally superior

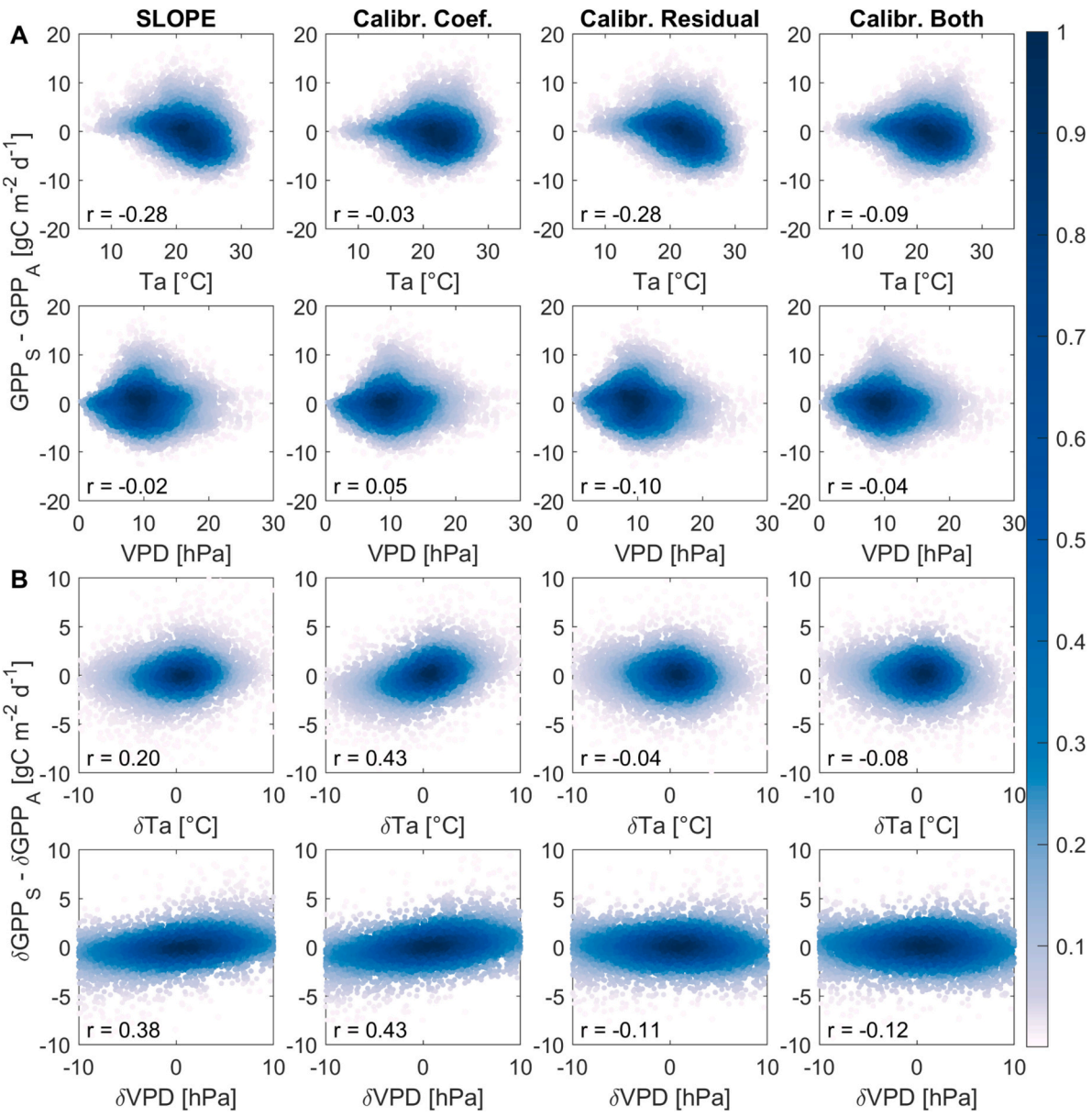

Fig. 5. Density scatter plot illustrates the relationship between the residual of SLOPE GPP and environmental factors of Ta and VPD, where the SLOPE model was performed with and without the coefficient calibration and/or residual calibration using all available data across C4 croplands.

to most others or at least has comparable performance with the best model in each PFT. In contrast, except for MOD17-NIRvP, none of the existing classical models can achieve the same consistently high performance as the ESLOPE model in the three PFTs. On the other hand, when comparing MOD17 (VPM) and MOD17-NIRvP (VPM-NIRvP), it was observed that incorporating NIRv into classic MOD17 and VPM models can typically improve their performance in most PFTs based on three error metrics. On average, the bias (RMSE) was reduced by 39 % (18 %) and 80 % (7 %) while the coefficient of determinant was increased by 24 % and 12 % for the MOD17 and VPM, respectively.

To further check their performance under stress conditions, we reproduced Fig. 9 considering only days with VPD $>$ 30 hPa for grasslands and Ta $<$ 15 °C for croplands. Consistent with Fig. 9, the results in Fig. 10 illustrate that the ESLOPE model generally performs better than other models under stress conditions for all three PFTs, in terms of bias, RMSE, and coefficient of determinant. Different from Fig. 9, we found that the bias of the ESLOPE model is significantly ($p < 0.01$) lower than most other models across three PFTs. In contrast, the biases of other models vary notably across different PFTs. Largely due to the low bias of the ESLOPE model, its RMSE remains at the lowest level among all models across the three PFTs. In terms of the correlation with measurements, although the coefficient of the determinant of the ESLOPE model is not the highest among different models but it has comparable performance with the best model for each PFT. On the other hand, Fig. 10 reaffirms that incorporating NIRv into classic MOD17 and VPM models can consistently improve their accuracy for all three PFTs under stress conditions based on three error metrics.

5. Discussion

5.1. Synthesis of the results for the science questions

In this study, we for the first time studied the effects of heat and moisture stress on the NIRvP-GPP relationship. Here, we summarize our main findings. First, we found that NIRvP cannot fully capture the plant response to Ta and VPD stress across grassland, C3 and C4 croplands.

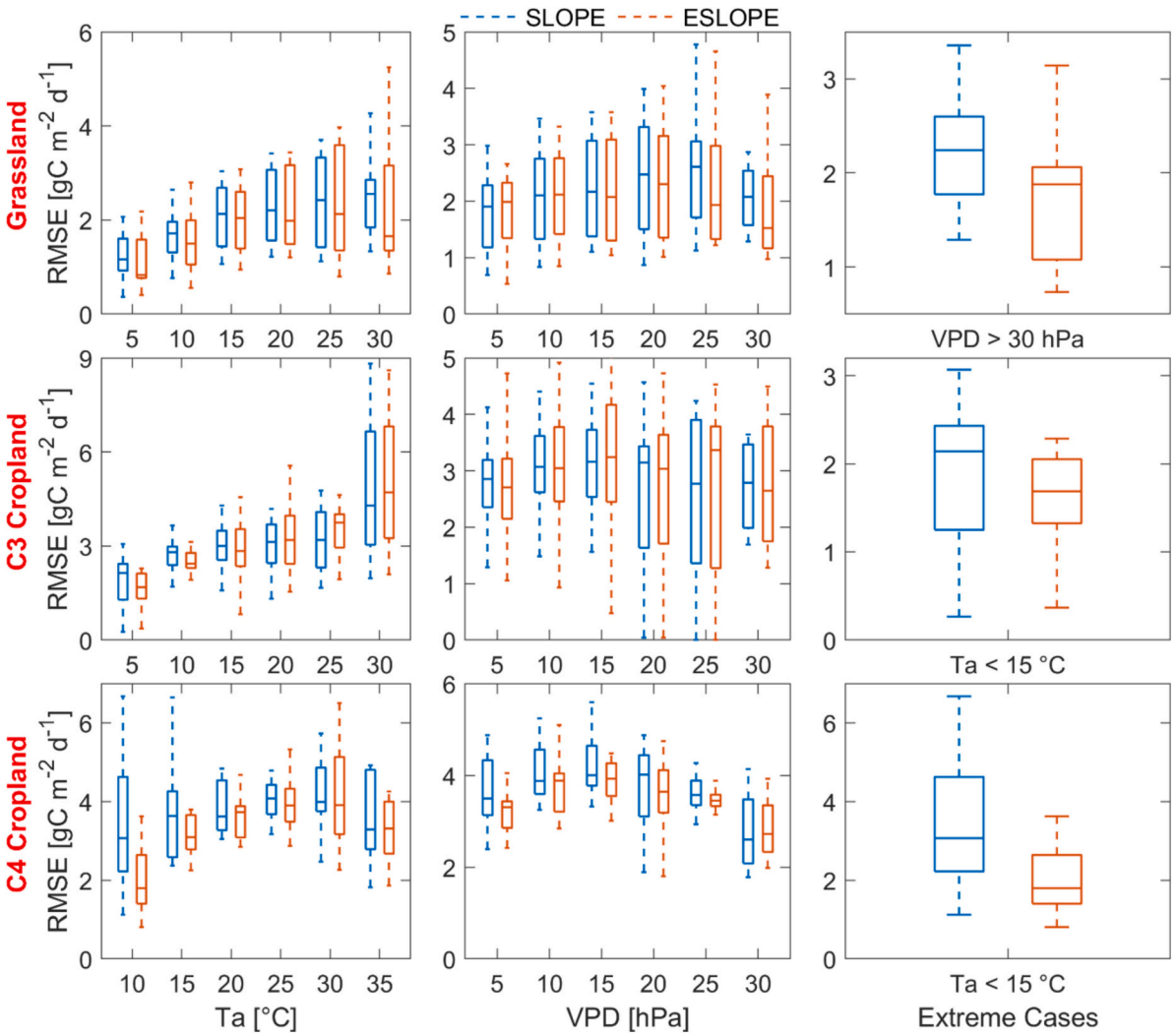

Fig. 6. Cross validation of SLOPE and ESLOPE GPP along Ta and VPD gradients and the extreme scenarios highlighted in Fig. 3. Data were categorized based on a 5 °C/hPa threshold around the central values within Ta and VPD gradients. The extreme scenario in grassland corresponds to Region A in Fig. 3, while it corresponds to Region B in Fig. 3 in croplands. The median is represented in each box, accompanied by the 25th and 75th percentiles with whiskers extending to 1.5 times the interquartile range around the median.

Specifically, the coefficient of the SLOPE model increased with Ta while decreased with VPD, indicating that NIRvP cannot well characterize the impact of environmental stress on GPP under extreme heat and moisture conditions. Second, the strong correlation between the differences in time-varying derivatives of NIRvP and EC GPP with Ta/VPD derivatives suggested that NIRvP cannot effectively capture the daily variations in GPP. Third, based on these analyses, we proposed an enhanced NIRvP model (i.e., ESLOPE) by simultaneously correcting its coefficient and daily-scale GPP variations using Ta and VPD. Fourth, when compared with other models — including LRC-NIRvP, MOD17, MOD17-NIRvP, VPM, VPM-NIRvP, and TL-LUE models — the results indicate that the ESLOPE model typically outperforms other models or at least has comparable performance with the best model in each PFT. Lastly, when comparing MOD17 and VPM to MOD17-NIRvP and VPM-NIRvP, we found that using the NIRv to parameterize FPAR term in classic one-leaf LUE models can notably improve their performance, indicating that NIRv is a better proxy of FPAR than traditional vegetation indices like EVI and LAI. This was further supported by the significantly higher coefficient of determinant between NIRv*PAR and EC GPP relative to those between $(1\text{-}e^{-0.5LAI})$*PAR (or EVI*PAR) and EC GPP across all three PFTs (Fig. 11). This is mainly because NIRv physically represents the amount of NIR light intercepted, scattered, and reflected by the vegetation structure, which not only partially eliminates the influence of the soil background but also closely reflects the interactions between solar radiation and the canopy, specifically the light interception and scattering processes (Badgley et al., 2017). By contrast, although EVI was designed to mitigate the soil background effects (Huete et al., 2002), it inherently denotes the vegetation greenness and cannot explicitly describe the interactions between light and vegetation structure. These results not only filled the knowledge gap on the impact of heat and moisture effects on the NIRvP-GPP relationship but also shed light on future improvements of LUE models given the outstanding performance of NIRv in characterizing vegetation structure.

5.2. Mechanism understanding

To better understand the mechanisms behind the results, we compared the LUE model (GPP_{LUE}), NIRv reflectance ($NIRv_{ref}$), NIRv radiance ($NIRv_{rad}$), and NIRvP (Badgley et al., 2017; Zeng et al., 2019; Dechant et al., 2020; Wu et al., 2020; Jiang et al., 2021). As shown in Fig. 12, we decomposed canopy-level observations of $NIRv_{ref}$, $NIRv_{rad}$, and NIRvP into leaf-level input variables based on the approach described by Zeng et al. (2019). Specifically, $NIRv_{ref}$ can be directly approximated by multiplying canopy interception, leaf single scattering

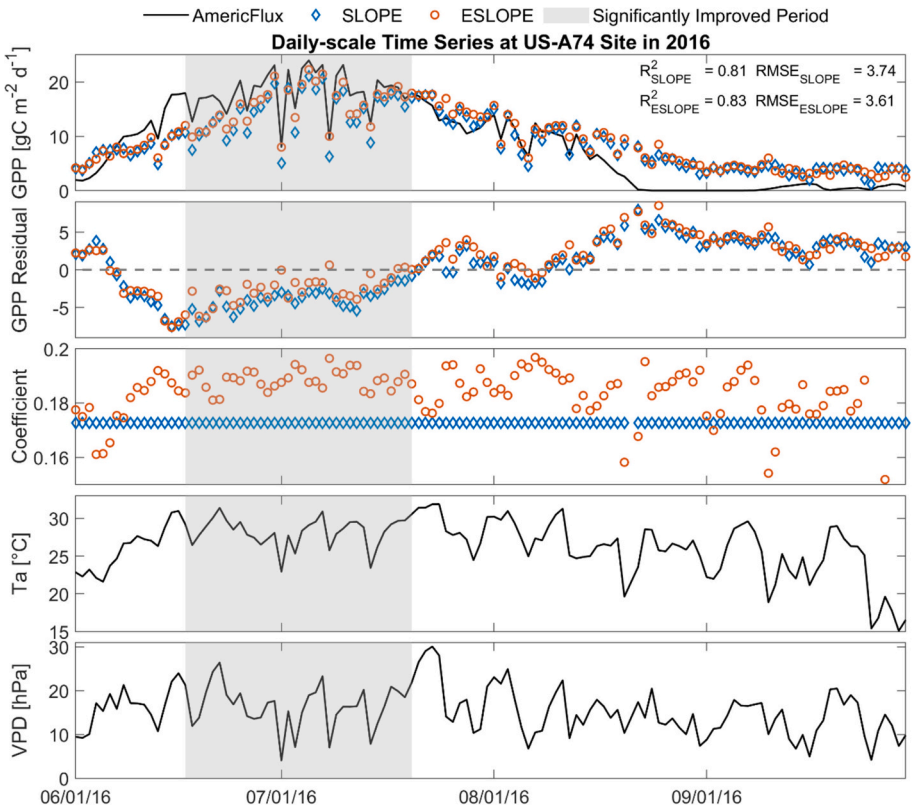

Fig. 7. Time-series of SLOPE and ESLOPE GPP, coefficient, daily mean Ta, and daily mean VPD at the US-A74 site (36.8°, −97.5°) during the peak growing season of C4 crop in 2016, where both models were calibrated using all available data across C4 cropland sites.

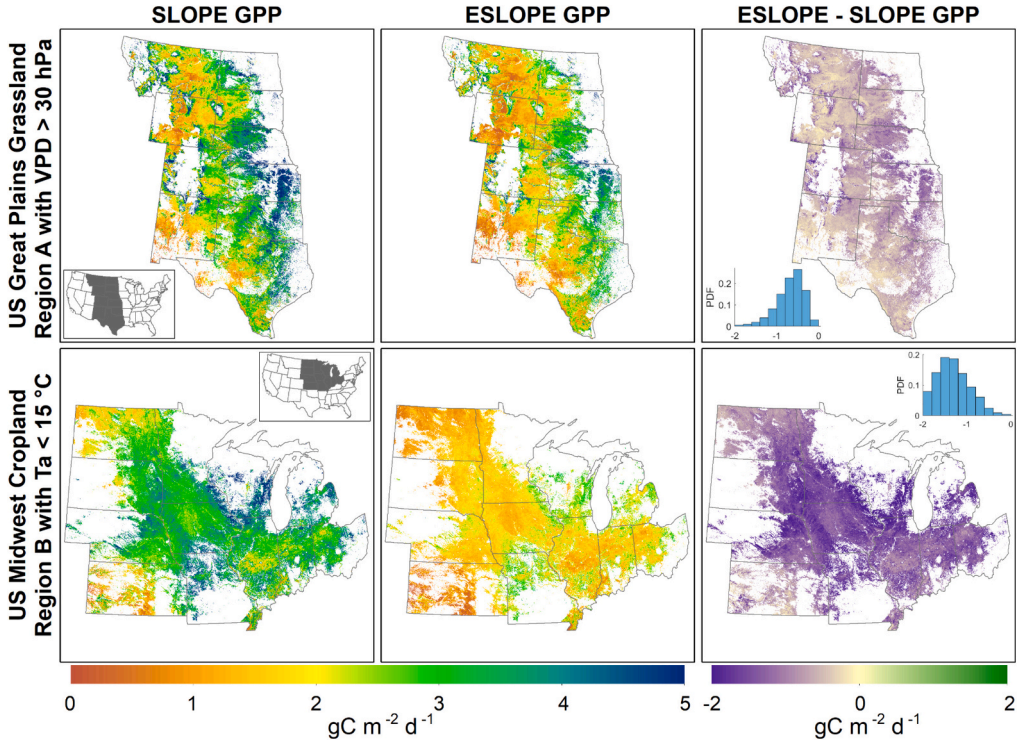

Fig. 8. Temporally averaged SLOPE and ESLOPE GPP and their difference across the US Great Plains and Midwest during the peak growing season from 2000 to 2019, where only days with VPD > 30 hPa were considered for grasslands while only days with Ta < 15 °C were considered for croplands. The extreme cases of VPD and Ta correspond to Regions A and B in Fig. 3.

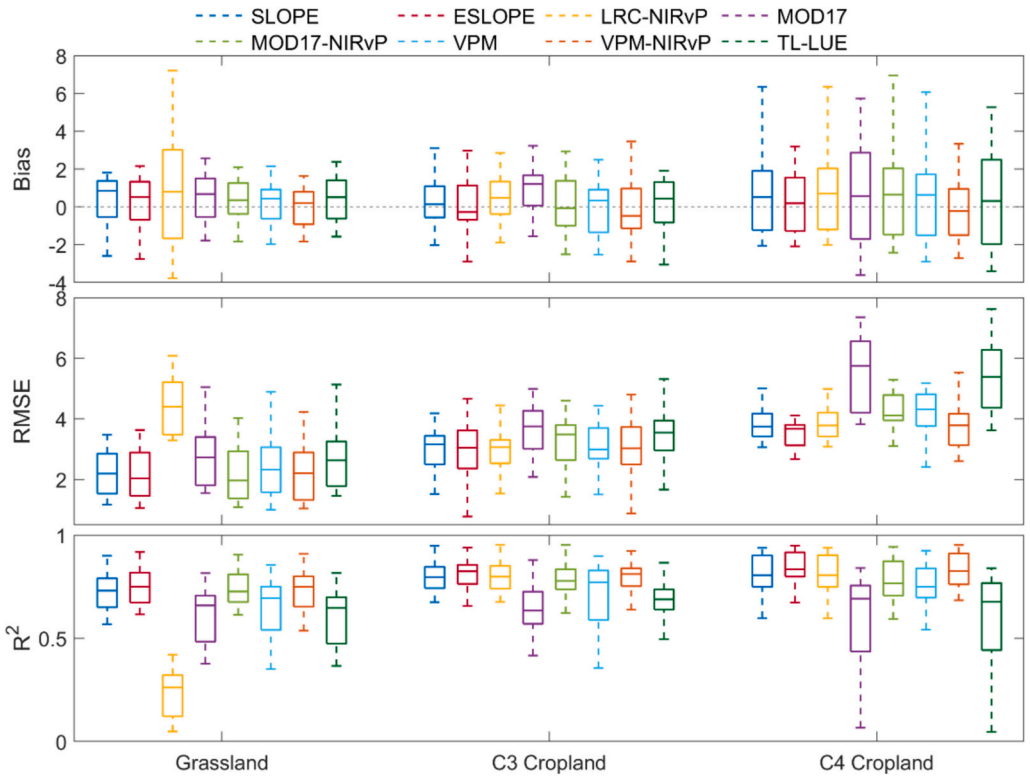

Fig. 9. Intercomparison between GPP estimates from SLOPE, ESLOPE, LRC-NIRvP, MOD17, MOD17-NIRvP, VPM, VPM-NIRvP, and TL-LUE models through level-one-site-out cross-validation using all available EC measurements across grasslands, C3 and C4 croplands. The median is represented in each box, accompanied by the 25th and 75th percentiles with whiskers extending to 1.5 times the interquartile range around the median.

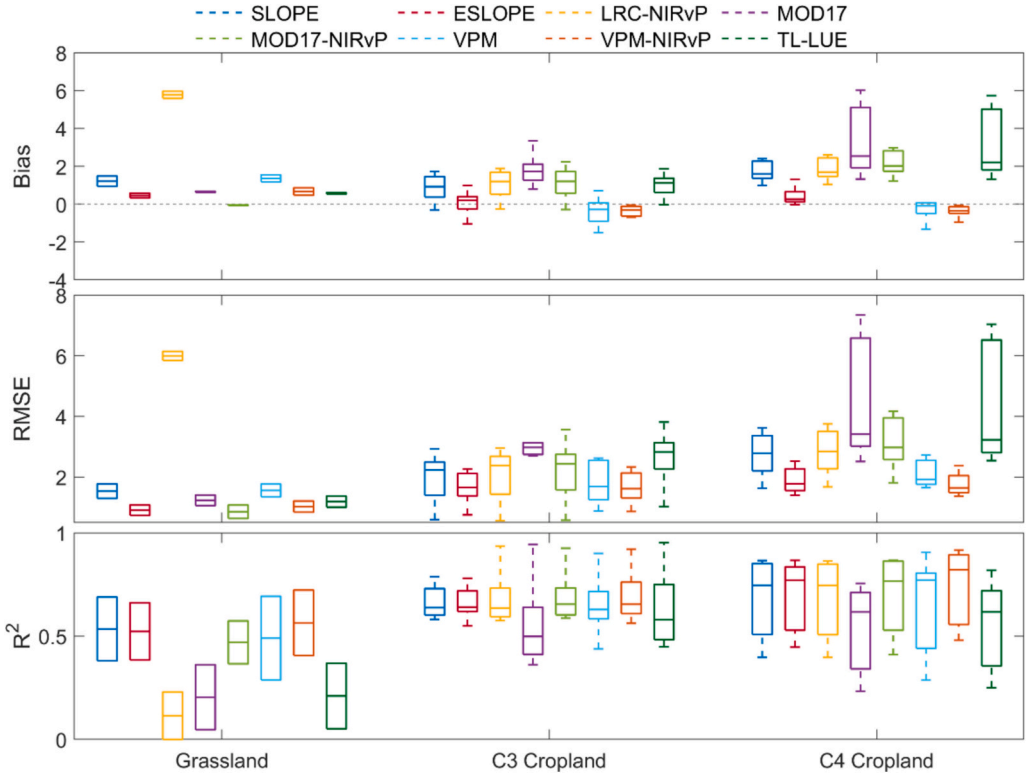

Fig. 10. Same as Fig. 9 but for stress conditions, where only days with VPD > 30 hPa were considered for grasslands while only days with Ta < 15 °C were considered for croplands.

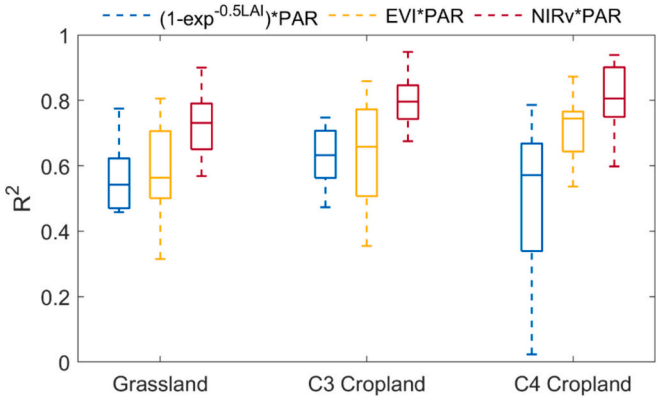

Fig. 11. Boxplot demonstrates the correlation between EC GPP and (1-$e^{-0.5LAI}$) *PAR or EVI*PAR or NIRv*PAR at EC sites across grassland, C3 and C4 croplands, where 1-$e^{-0.5LAI}$ is the key component of MOD17 FPAR. The ANOVA test indicates that NIRv*PAR has a significantly stronger correlation with EC GPP compared to others ($p < 0.01$).

$$GPP_{LUE} = PAR \cdot fPAR \cdot LUE$$
$$NIRv_{ref} = i_0 \cdot \omega \cdot f_{esc}$$
$$NIRv_{rad} = S_{760} \cdot i_0 \cdot \omega \cdot f_{esc}$$
$$NIRvP = PAR \cdot i_0 \cdot \omega \cdot f_{esc}$$

Fig. 12. Schematic overviews of the LUE model (GPP_{LUE}), NIRv reflectance ($NIRv_{ref}$), and NIRv radiance ($NIRv_{rad}$), and NIRvP where i_0, ω, f_{esc}, and S_{760} represent canopy interception, leaf single scattering albedo, escaping ratio, and the incoming solar radiation flux at 760 nm, respectively.

albedo, and escaping ratio. $NIRv_{rad}$ is the product of these factors with the addition of incoming solar radiation flux at 760 nm while NIRvP is the product of these factors with PAR.

Fig. 12 demonstrates that $NIRv_{rad}$ and NIRvP share similar components, and by their nature, they are expected to perform better than $NIRv_{ref}$ in estimating GPP since they incorporate solar radiation information in addition to plant biophysical information. This result is consistent with the previous findings by Wu et al. (2020) and Dechant et al. (2020). On the other hand, when comparing NIRvP and GPP_{LUE}, the high performance of NIRvP is attributed to its ability to explain fPAR and partly incorporate the LUE stress term through factors like canopy interceptance, leaf single scattering albedo, and escaping ratio. These factors are significantly related to vegetation structure (Yang and van der Tol, 2018), which adjusts to environmental stress at a long-term time scale (Hikosaka and Hirose, 1997; Yamori et al., 2010). However, only using vegetation structure-dependent variables falls short in capturing other LUE stress term variations under stressed conditions, especially on a daily basis, such as the instantaneous stomata response to environmental stress (Farquhar and Von Caemmerer, 1982; Leuning, 1995). Hence, integrating environmental variables such as water and heat stresses with NIRvP is essential for a more accurate estimation of GPP, as it helps to account for the dynamic interplay between environmental stressors and gas exchange processes within the vegetation canopy.

5.3. Further consideration of uncertainties and possible improvement

Although a notable improvement in the SLOPE model was observed after incorporating Ta and VPD, some limitations should be taken into account when interpreting our results. In this study, we only used the AmeriFlux sites where the coefficient of determination between NIRv and measured GPP was greater than 0.5 considering the moderate to high correlation between NIRv and GPP (Badgley et al., 2017) and the EC representativeness issue (Barcza et al., 2009; Chen et al., 2012). Typically, the EC footprint can extend up to a 1000-m radius around a flux tower (Kumar et al., 2016; Chu et al., 2021), which is much larger than the 250-m NIRv observations from MODIS. In this scenario, MODIS satellite observations are unable to fully capture the spatial heterogeneity within an EC footprint. Taking the US-Bd4 crop site as an example, where the flux tower is situated between two neighboring rice fields, the correlation coefficient between EC GPP and corresponding NIRv observations is less than −0.1 using data during the peak growing season in 2005 and 2006. This discrepancy occurs because the EC measurements and NIRv represent two different fields with distinct crop phenology, as we examined (not shown here). Therefore, using the coefficient of determination threshold between NIRv and measured GPP allows us to mitigate representativeness issue. On the other hand, to check whether the mixture of C3 and C4 plant has a significant impact on our analysis, we reproduced the results using only pure satellite pixels without C4/C3 plant admixture based on the 30-m CDL data. Figs. G1 & G2 in Appendix show quite consistent results with Figs. 2 & 9, indicating the robustness of our analysis. Besides, we acknowledge that this representativeness issue may also be alleviated using high-resolution data from Sentinel-2 or Landsat satellites or the Harmonized Landsat and Sentinel (HLS) products (Pabon-Moreno et al., 2022; Kong et al., 2022; Chen et al., 2023).

On the other hand, for the quantification of the Ta and VPD effects on the SLOPE model, we used the PAR estimations from the shortwave radiation measurements obtained from AmeriFlux sites rather than estimates from the SLOPE datasets (Jiang and Guan, 2020) to avoid possible uncertainties propagating from numerous forcing data into PAR (Section 2.2). This is because shortwave radiation exhibits a strong correlation with PAR (Liang and Wang, 2019) and its measurements are effective in reflecting daily variabilities in PAR. In addition, we corrected the VPD effects using an exponential decay function without considering an interception term (Eq. (2b)), which could lead to a notable deviation between binned and approximated SLOPE coefficients (Fig. 3). While incorporating an intercept term into the exponential decay function of VPD could result in a more accurate approximation of SLOPE coefficients that align better with the binned values at lower VPD levels. However, our study revealed that this modification does not significantly impact the cross-validation results but could introduce more uncertainty since more unknowns need to be calibrated. Moreover, it is noted that when accounting for moisture effects in the SLOPE model, we used VPD that can well represent the impact of atmospheric dryness on plant photosynthesis while not considering soil moisture conditions due to the lack of long-term high-resolution products for the implementation of the ESLOPE model at regional scales (Gao et al., 2020; Gao et al., 2021; Gao et al., 2022). However, we note that soil moisture is essential for plant photosynthesis by modulating stomatal conductance and leaf cell turgor pressure (Leuning et al., 2005) and that failure to consider soil moisture may lead to notable GPP underestimation (Stocker et al., 2018, 2019). Thus, future works are still encouraged to further improve the ESLOPE model when high-resolution data are available.

In addition, we restricted our analysis to the US Great Plains pasturelands and Midwest croplands during the peak growing season, considering (1) the importance of the Great Plains grasslands and Midwest croplands to US and global agriculture (Drummond et al., 2012; Hatfield, 2012; Heinemann et al., 2014; USDA NASS, 2018), (2) the substantial water and heat gradients in this region (Beck et al., 2018), and (3) the notable effects of moisture and heat on controlling ecosystem fluxes during the peak growing season (Liu et al., 2020a; Wang et al., 2022; Gao et al., 2024). We note that future efforts are still needed to expand to other ecosystems and across seasons. Furthermore, this work mainly used MOD09 surface reflectance products for NIRv calculation rather than BRDF-corrected reflectance considering the following reasons. First, the used NIRv dataset was well constructed and published (Jiang and Guan, 2020), which has also been extensively examined in estimating GPP across US (Jiang et al., 2021). Second, as pointed by Doughty et al. (2021), unadjusted NIRv was more coherent with plant photosynthesis-dependent SIF at mid and high latitude than BRDF-adjusted NIRv. Third, the BRDF correction for MODIS reflectance could introduce additional uncertainties in calculating NIRv since it assumes the surface is homogeneous and only limited number of viewing angles are available for BRDF correction (Schaaf et al., 2002). Lastly, as we examined at two randomly selected EC sites (i.e., US-AR1 and US-IB1), the used NIRv has higher correlations with EC GPP than BRDF-corrected NIRv from the MCD43C4 product. Nonetheless, we acknowledge that correcting for BRDF could be necessary when forests are involved across globe scales (Huang et al., 2019).

Despite these limitations, it is expected that this work has implications for future GPP studies beyond the current findings. Several studies strived to estimate the regional or global GPP using $NIRv_{rad}$ or $NIRv_{ref}$ (Badgley et al., 2019; Liu et al., 2020c; Wang et al., 2020a; Wang et al., 2021). In these studies, they directly used EC measurements to benchmark the satellite-observed NIRvP without accounting for the water and heat stressors. Consequently, this may lead to a notable bias of GPP during extreme Ta and VPD conditions, as indicated by our findings. The same caveat is also applicable to those research endeavors that directly employed NIRvP as a proxy for GPP to identify seasonal and yearly fluctuations in GPP, as well as to observe how GPP responds to challenges like drought, heatwaves, and tropospheric ozone (Wang et al., 2020b; Wang et al., 2020c; Yang et al., 2022; Gao et al., 2024). Therefore, there is a potential for further improvements in those GPP estimations or their response to environmental factors when the effects of environmental stressors are corrected. Nevertheless, it is important to note that calibrating unknown variables in Eq. (2) might pose greater complexities in global studies compared to regional ones. This complexity arises from the fact that GPP tends to show more consistent variability at a regional scale with the same PFT and climate regime. To enhance accuracy in regional and/or global studies, it would be beneficial to simultaneously account for plant conditions and climate types when calibrating the unknowns in Eqs. (5)–(7). Considering that the ESLOPE model shares similar algorithmic structures with other one-leaf LUE models and that the ESLOPE model performs better than MOD17 and VPM models across three reported PFTs, it is expected that NIRvP may serve as a viable alternative vegetation index for enhancing these models.

6. Conclusions

For improving GPP estimates, this study examined and integrated the effects of heat and water stress into the SLOPE model that calculates GPP as a product of a plant-type-specific coefficient and NIRvP. This investigation was carried out across the US Great Plains pasturelands and Midwest croplands. Specifically, we initially analyzed the effects of Ta and VPD on both the SLOPE coefficient and GPP changing rate. The binning analysis revealed that SLOPE coefficients exhibited a notable increase with Ta and a decrease with VPD. This relationship could result in a substantial divergence between GPP estimates and EC measurements, particularly under extreme Ta and VPD conditions. Additionally, our investigation revealed that the disparity between the changing rates of SLOPE and EC GPP was notably influenced by the time-varying derivatives of both Ta and VPD since NIRvP cannot fully explain the day-to-day fluctuations in GPP with Ta and VPD. Subsequently, an enhanced version of the model was proposed through the correction of its coefficients and day-to-day variation. To incorporate the Ta and VPD effects into the SLOPE model, we calibrated the SLOPE coefficient using a polynomial function of Ta and an exponential function of VPD while the day-to-day GPP variations were corrected using a linear function of Ta and VPD. The cross-validation results demonstrated that under extremely low Ta and high VPD conditions, ESLOPE could notably improve GPP accuracy for grasslands, C3 and C4 croplands compared with SLOPE model. On the other hand, we inter-compared the ESOLPE model with six other models, including LRC-NIRvP, MOD17, MOD17-NIRvP, VPM, VPM-NIRvP, and TL-LUE models. It was observed that ESLOPE generally performed better than others or at least had equivalent performance with the best model in terms of bias, RSME and coefficient of determinant with EC measurements across different PFTs. In addition, the results revealed that directly parameterizing FPAR term using NIRv for classic MOD17 and VPM models can notably improve their performance. Overall, this study not only quantified and accounted for the impacts of Ta and VPD on the NIRvP-GPP relationship but also demonstrated the advantages of using NIRvP to improve the classic LUE models.

CRediT authorship contribution statement

Lun Gao: Writing – review & editing, Writing – original draft, Visualization, Validation, Methodology, Investigation, Formal analysis, Data curation, Conceptualization. **Kaiyu Guan:** Writing – review & editing, Writing – original draft, Visualization, Validation, Supervision, Resources, Project administration, Methodology, Funding acquisition, Formal analysis, Conceptualization. **Chongya Jiang:** Writing – original draft, Methodology, Formal analysis. **Xiaoman Lu:** Writing – original draft, Formal analysis. **Sheng Wang:** Writing – original draft. **Elizabeth A. Ainsworth:** Writing – original draft, Methodology, Formal analysis. **Xiaocui Wu:** Writing – original draft, Formal analysis. **Min Chen:** Writing – original draft.

Declaration of competing interest

The authors declare that they have no known competing financial interests or personal relationships that could have appeared to influence the work reported in this paper.

Acknowledgments

This work was supported by the National Science Foundation (NSF) Career Award (1847334), NASA Carbon Monitoring System, the USDA NIFA's AIFARMS project, and the support from the Agroecosystem Sustainability Center of UIUC. The authors also highly appreciated the early discussion with Dr. Dennis Baldocchi at the University of California, Berkeley.

Appendix A. Occurrences of Ta and VPD extremes during Peak growing season

To assess occurrences of extremely low and high Ta and VPD, we generated a time series plot depicting the minimum and maximum ranges of Ta and VPD using all PRISM data across available AmeriFlux sites in US Great Plains and Midwest. As illustrated in Fig. A1, Ta values below 10 °C tend to manifest during the early or late stages of the growing seasons, specifically in June and September. Conversely, high Ta values around 30 °C can be observed throughout virtually the entire growing season. Concerning VPD, the minimum value consistently hovers near 0 hPa, whereas high VPD values exceeding 30 hPa can sporadically materialize during the growing season, particularly in July and August. On the other hand, Fig. A1 illustrates that PRISM Ta and VPD are highly correlated with AmeriFlux achieved ERA-Interim values with the coefficient of determination all greater than 0.85. This robust correlation suggests that both datasets are suitable for providing reliable analysis in the main text.

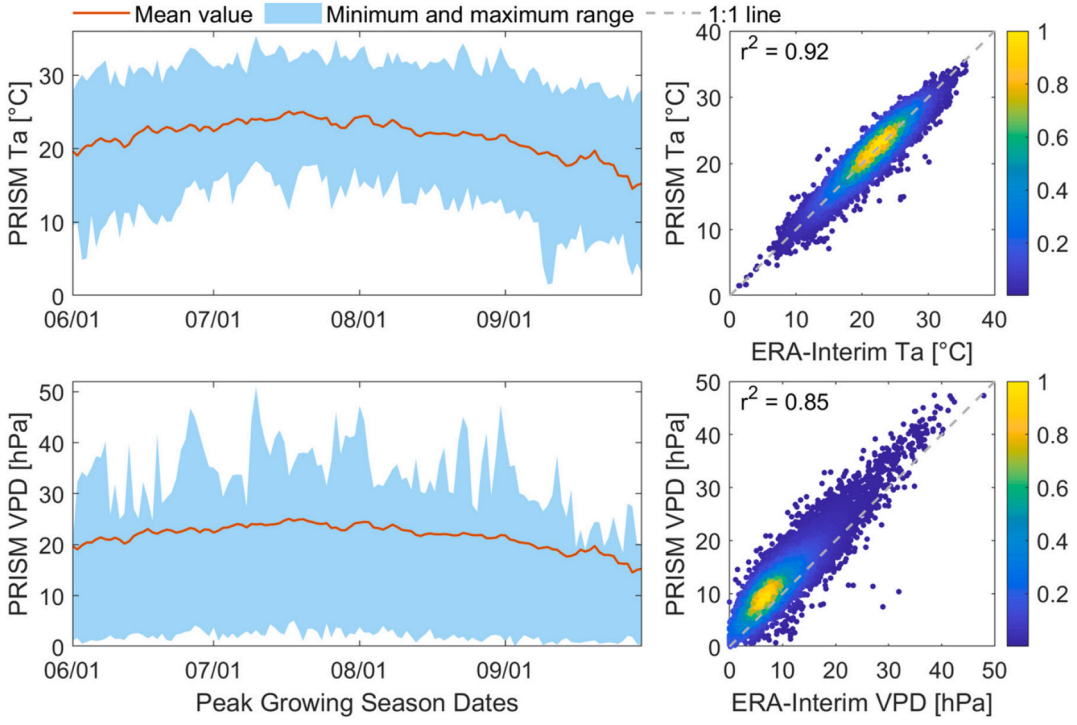

Fig. A1. Time series of minimum and maximum ranges of Ta and VPD during the peak growing season using all available PRISM data across AmeriFlux sites as well as the density scatter plot demonstrating the correlation between PRISM and AmeriFlux achieved ERA-Interim Ta and VPD.

Appendix B. Spatial representativeness of selected EC sites

To evaluate the spatial representativeness of selected EC sites, we examined the percentage of the dominant land cover type within the 250-m radial distance from the tower using the 30-m CDL land cover, where the specific radius was determined to be consistent with (Chu et al., 2021) as well as the 250-m MODIS footprint size used. Note that only available sites during 2008 and 2019 were considered due to the availability of CDL data. The results in Fig. B1 demonstrate that most sites had high spatial representativeness with more than 80 % of the dominant land cover within the 250-m radial distance from the tower across three PFTs, especially for C3 and C4 cropland sites. However, we also observed a few less represented EC sites with dominant land cover notably below 50 % within a 250-m radial distance from the tower, such as US-A32, US-AR2, and US-IB2. As we checked per site, this is partly because the reported land cover is concentrated at smaller radial distances from the tower, such as US-A32, which nevertheless overlaps well with 250-m MODIS coverage. On the other hand, it is because of the inaccuracies in CDL data, which misclassifies grassland as others, such as US-AR2 and US-IB2. Overall, the selected sites have moderate to high spatial representation.

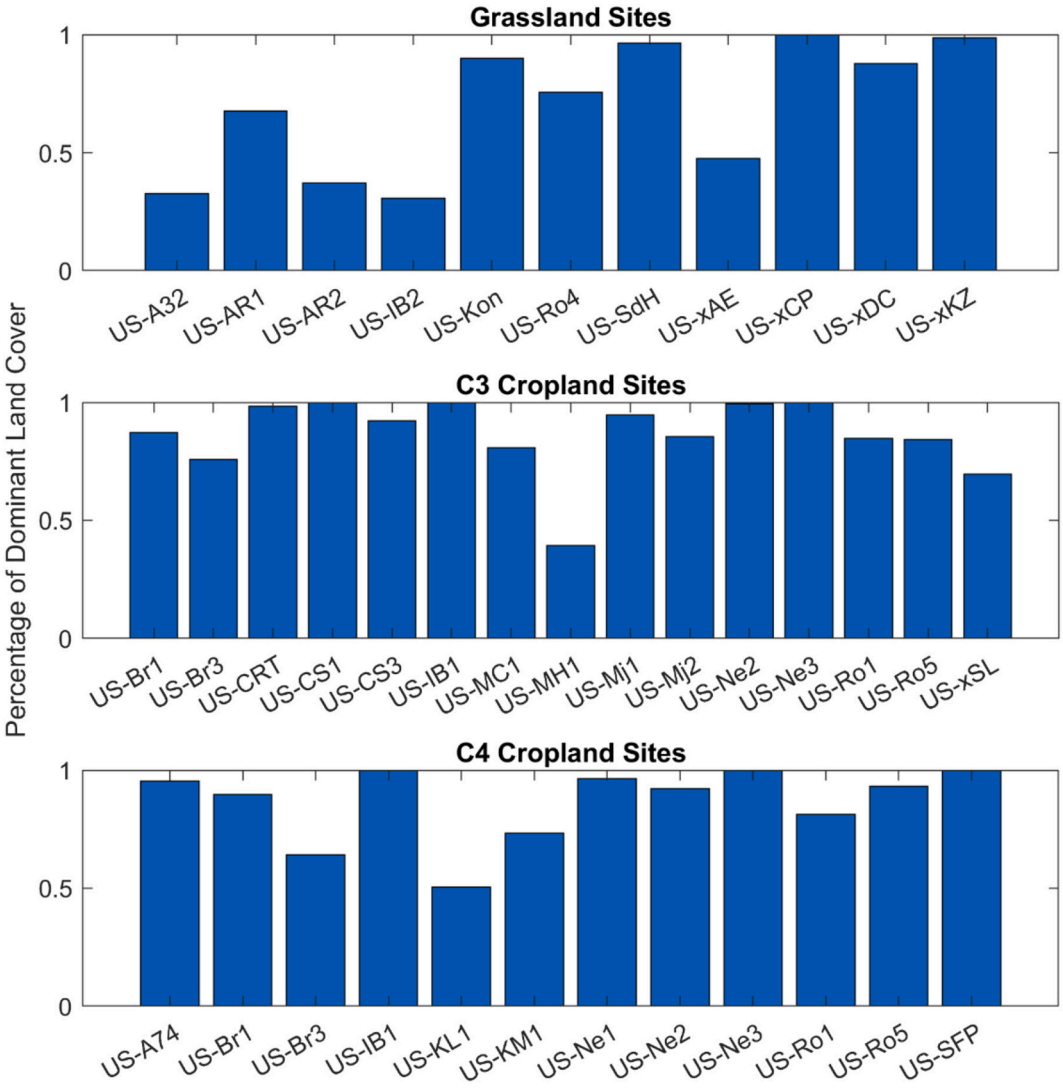

Fig. B1. Spatial representativeness of EC site using 30-m CDL land covers from 2008 to 2019.

Appendix C. Specifications of other GPP models

C.1. LRC-NIRvP model

LRC-NIRvP was first proposed by Khan et al. (2022) based on the light response curve that can partition net ecosystem exchange (NEE) into GPP and ecosystem respiration (Lasslop et al., 2010). It is expressed as

$$GPP = \frac{\gamma \bullet NIRvP \bullet \eta}{\gamma \bullet NIRvP + \eta} \tag{3}$$

in which γ (μmol CO_2 J^{-1}) denotes the canopy-level LUE prior to reaching light saturation and η represents the maximum canopy CO_2 uptake rate at the light saturation point (Lasslop et al., 2010; Reichstein et al., 2012). Note that γ and η are approximated using the least-square regression method based on eddy covariance measurements for each PFT.

C.2. MOD17 and MOD17-NIRvP models

The classic MOD17 model is directly derived from Monteith's LUE concept (Monteith, 1972, 1977), which has been routinely used to produce MODIS GPP products (Running et al., 1999). Specifically, FPAR is parameterized as an exponential decay function of LAI while LUE is simultaneously constrained by linear ramp functions of Ta and VPD. The formulas are described as follows:

$$GPP = \varepsilon_{max} \bullet PAR \bullet FPAR \bullet W_s \bullet T_s \tag{4a}$$

$$FPAR = 0.95 \bullet \left(1 - e^{-k \bullet LAI}\right) \tag{4b}$$

$$W_s = \begin{cases} 1, VPD \le VPD_{min} \\ \dfrac{VPD_{max} - VPD}{VPD_{max} - VPD_{min}}, VPD_{min} < VPD < VPD_{max} \\ 0, VPD \ge VPD_{max} \end{cases} \tag{4c}$$

$$T_s = \begin{cases} 0, T \le T_{min} \\ \dfrac{T - T_{min}}{T_{max} - T_{min}}, T_{min} < T < T_{max} \\ 1, T \ge T_{max} \end{cases} \tag{4d}$$

where ε_{max} is the maximum LUE, which is downregulated by water stress (W_s) and temperature stress (T_s); $k = 0.5$ is the light extinction coefficient (Leverenz and Jarvis, 1980); VPD_{min} and VPD_{max} are daily minimum and maximum VPD (hPa); T_{min}, and T_{max} are daily minimum and maximum Ta (°C). ε_{max} was determined through least square regression using all EC measurements for each PFT while the PFT-specific values of VPD_{min}, VPD_{max}, T_{min}, and T_{max} are directly obtained from MODIS user's guide (Running and Zhao, 2019), which are also provided in Table 3. Adapted from the MOD17 model, the MOD17-NIRvP model has the same expressions as the MOD17 model, but with the FPAR term set equal to NIRv.

C.3. VPM and VPM-NIRvP models

Like the MOD17 algorithm, the VPM model (Xiao et al., 2004a; Xiao et al., 2004b) parameterizes FPAR with a vegetation index while its maximum LUE (ε_{max}) is scaled by water and heat stresses but with a different parameterization scheme (Raich et al., 1991):

$$GPP = \varepsilon_{max} \bullet PAR \bullet FPAR \bullet W_s \bullet T_s \tag{5a}$$

$$FPAR = 1.25 \bullet (EVI - 0.1) \tag{5b}$$

$$W_s = \frac{1 + LSWI}{1 + LSWI_{max}} \tag{5c}$$

$$T_s = \begin{cases} 0, T \le T_{min} \text{ or } T \ge T_{max} \\ \dfrac{(T - T_{min})(T - T_{max})}{(T - T_{min})(T - T_{max}) - \left(T - T_{opt}\right)^2}, T_{min} < T < T_{max} \end{cases} \tag{5d}$$

where EVI is adjusted with constants of 1.25 and 0.1 to circumvent the effects of sparsely vegetated areas (Wu et al., 2018); The $LSWI_{max}$ is the multi-year maximum LSWI value. T_{min}, T_{max}, and T_{opt} represent the PFT-dependent minimum, maximum, and optimum temperatures, which were directly adopted from Zhang et al. (2017) and are available in Table 3. Similar to the MOD17 model, ε_{max} was specified through the least square regression calibration based on EC measurements across different PFTs while W_s and T_s range from 0 to 1 with larger values denoting less stressed cases. Adapted from the VPM, the VPM-NIRvP model has the same formula as VPM but its FPAR term is set to be equal to NIRv.

C.4. TL-LUE model

Stemmed from the MOD17 and the process-based boreal ecosystem productivity simulator (BEPS) (Chen et al., 1999), the TL-LUE model divides the canopy into sunlit and shaded leaves (He et al., 2013; Wu et al., 2015; Zhou et al., 2016), considering that diffuse radiation can contribute significantly to plant photosynthesis (Roderick et al., 2001; Mercado et al., 2009; Oliphant et al., 2011). The TL-LUE model calculates GPP as follows:

$$GPP = \left(\varepsilon_{msu} \bullet APAR_{su} + \varepsilon_{msh} \bullet APAR_{sh}\right) \bullet W_s \bullet T_s \tag{6a}$$

$$APAR_{su} = (1 - \omega) \bullet \left(PAR_{dir} \bullet \frac{\cos \varphi}{\cos \theta} + \frac{PAR_{dif} - PAR_{dif,u}}{LAI} + C\right) \bullet LAI_{su} \tag{6b}$$

$$APAR_{sh} = (1 - \omega) \bullet \left(\frac{PAR_{dif} - PAR_{dif,u}}{LAI} + C\right) \bullet LAI_{sh} \tag{6c}$$

$$W_s = \begin{cases} 1, VPD \le VPD_{min} \\ \dfrac{VPD_{max} - VPD}{VPD_{max} - VPD_{min}}, VPD_{min} < VPD < VPD_{max} \\ 0, VPD \ge VPD_{max} \end{cases} \tag{6d}$$

$$T_s = \begin{cases} 0, T \le T_{min} \\ \dfrac{T - T_{min}}{T_{max} - T_{min}}, T_{min} < T < T_{max} \\ 1, T \ge T_{max} \end{cases} \quad (6e)$$

$$PAR_{dir} = PAR - PAR_{dif} \quad (6f)$$

$$PAR_{dif} = PAR \bullet \left(0.7527 + 3.8453 \bullet R - 16.316 \bullet R^2 + 18.962 \bullet R^3 - 7.0802 \bullet R^4\right) \quad (6g)$$

$$PAR_{dif,u} = PAR_{dif} \bullet e^{-0.5 \bullet \Omega \bullet \frac{LAI}{\cos\theta}} \quad (6h)$$

$$C = 0.07 \bullet \Omega \bullet PAR_{dir} \bullet (1.1 - 0.1 \bullet LAI) \bullet e^{\cos\theta} \quad (6i)$$

$$LAI_{su} = 2 \bullet cos\theta \bullet \left(1 - e^{-0.5 \bullet \Omega \bullet \frac{LAI}{\cos\theta}}\right) \quad (6j)$$

$$LAI_{sh} = LAI - LAI_{su} \quad (6k)$$

where ε_{msu} and ε_{msh} denote the maximum LUE for sunlit and shaded leaves; ω is the canopy albedo; PAR_{dir}, PAR_{dif}, and $PAR_{dif,u}$ are the direct component of incoming PAR, diffuse component of incoming PAR, and diffuse PAR under the canopy (Chen et al., 1999); $\frac{PAR_{dif} - PAR_{dif,u}}{LAI}$ stands for the diffuse PAR per unit leaf area below the canopy; $R = PAR/(PAR/0.5S_0 cos\theta)$ is the sky clearness index with $S_0 = 1367$ W m^{-2} as a solar constant; C quantifies the multiple scattering of direct radiation to the diffuse irradiance (Norman, 1982); $\varphi = 60^{\circ}$ is the mean leaf-sun angle; θ is the solar zenith angle; LAI_{su} and LAI_{sh} represent the sunlit and shaded LAI; Ω is the clumping index. Note that the values for ε_{msu}, ε_{msh}, ω, and Ω were calibrated using the least-square regression based on all available EC measurements for each PFT, which are provided in Table 3.

Table 3

Specifications of PFT-specific T_{min}, T_{max}, T_{opt}, VPD_{min}, VPD_{max}, ε_{msu}, ε_{msh}, ω, and Ω for MOD17, VPM, and TL-LUE models, where MOD17 and VPM related values can refer to (Running and Zhao, 2019; Zhang et al., 2017) while the last four parameters for the TL-LUE model were optimized based on all available EC measurements. Note that VPM values are marked with a superscript of '*'.

PFT	Grassland	C3 Cropland	C4 Cropland
T_{min} (°C)	−8 (0*)	−8 (−1*)	
T_{max} (°C)	12.02 (48*)	12.02 (48*)	
T_{opt} (°C)	27*	30*	
VPD_{min} (hPa)	6.5	6.5	
VPD_{max} (hPa)	53	43	
ε_{msu} (gC/MJ)	0.96	0.85	1.36
ε_{msh} (gC/MJ)	2.15	4.88	5.27
ω	0.23	0.47	0.43
Ω	0.9	1.69	1.11

Appendix D. Quantification of Ta and VPD impacts on SLOPE GPP

As a complementary to Fig. 2, we also investigated the SLOPE coefficient at different levels of Ta and VPD by binning data using daily maximum Ta and VPD. Consistent with Fig. 2, Fig. D1 demonstrates that the SLOPE coefficient increases with Ta for C3 and C4 croplands and decreases with enhanced VPD for all three PFTs. However, we note that the SLOPE coefficient exhibits remarkable fluctuations when the daily maximum Ta is less than 15 °C or when the daily maximum VPD hovers near 0 hPa. This is probably because daily maximum Ta and VPD exert a more significant influence on the GPP variation when Ta and VPD are relatively high in contrast to when they are relatively low.

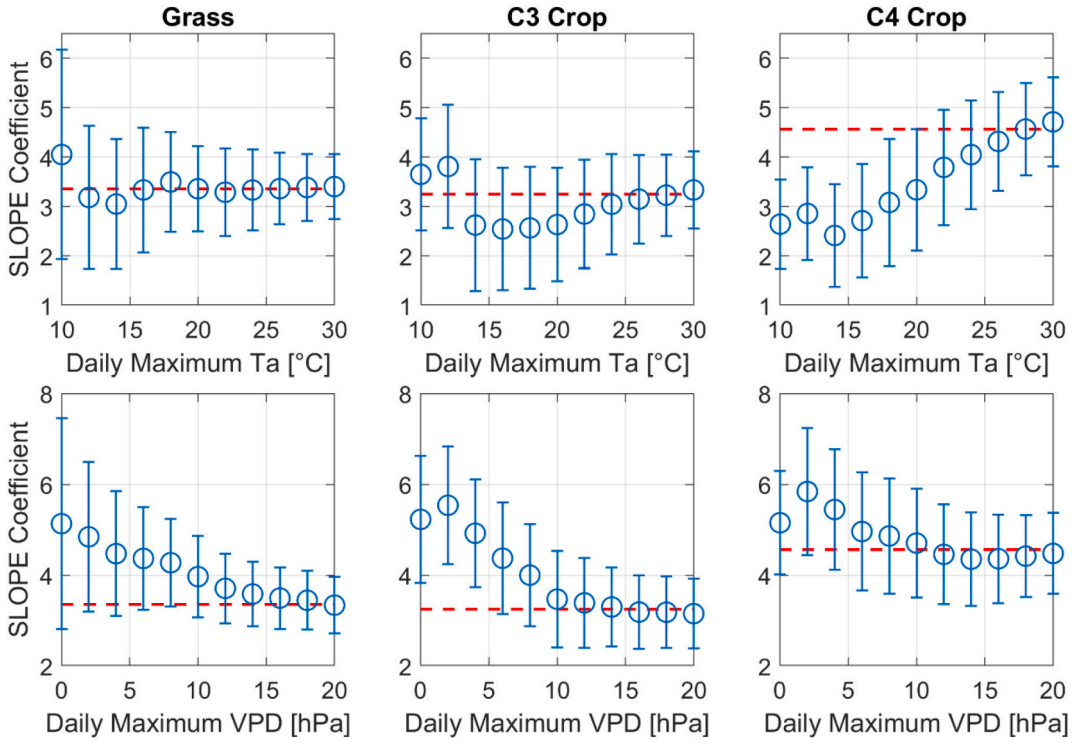

Fig. D1. Same as Fig. 2 but data were binned by daily maximum Ta and VPD.

The results in Fig. D2 reaffirm there exists a notable correlation between δGPP_S - δGPP_A and the daily mean Ta and VPD across all land cover types. When compared with Fig. 4, the correlation between δGPP_S - δGPP_A and daily mean VPD derivatives remains at the same level as that using daily maximum VPD derivatives. However, the correlation between δGPP_S - δGPP_A and the daily mean Ta is significantly lower than that using daily maximum Ta derivatives. This is primarily due to the fact that daily mean Ta has the tendency to incorporate information from both the daily minimum and maximum values, as both of these values exhibit significant fluctuations across days. However, this is not the case for VPD, as the daily minimum VPD remains relatively consistent across days.

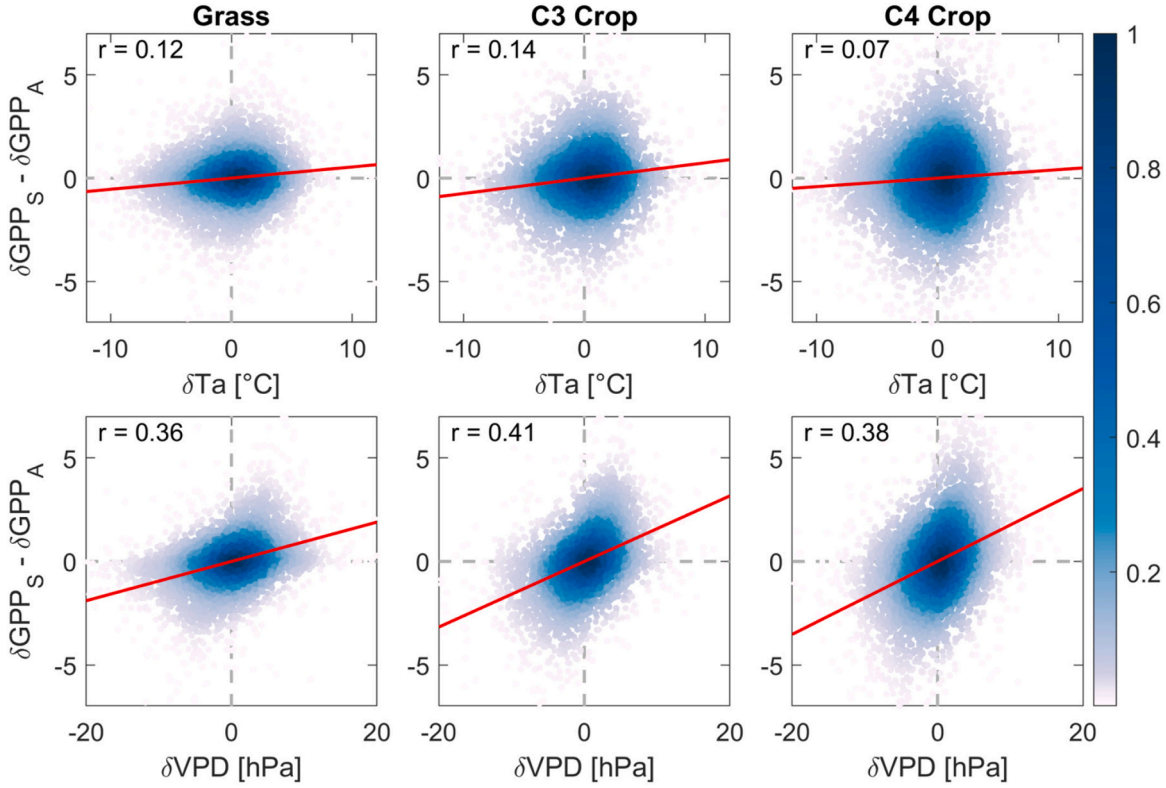

Fig. D2. Same as Fig. 4 but using the time-varying derivatives of daily mean Ta (δTa) and VPD (δVPD).

Appendix E. Effects of calibration procedures on the coupling between SLOPE GPP and stress

As complementary to Fig. 5, Figs. E1 & E2 demonstrate the correlation between the calibrated GPP residual and stress and the correlation between the deviation of the time-varying derivative of calibrated GPP from the measured values and the corresponding derivatives of Ta and VPD across grasslands and C3 croplands. Consistent with the findings in Fig. 5, the results here reaffirmed that the joint calibration of both the SLOPE coefficient and GPP daily-scale changing rate can more effectively mitigate the reliance of GPP estimations on environmental stress factors of Ta and VPD compared to solely calibrating the SLOPE coefficient or GPP daily-scale changing rate individually. To be specific, directly calibrating the SLOPE coefficient can reduce the correlation between the calibrated GPP residual and stress, while it only has a limited impact on the relationship between the deviation of the time-varying derivative of calibrated GPP from the measured values and the corresponding derivatives of Ta and VPD. On the other hand, the direct calibration of the GPP rate can notably decrease the coupling between the deviation of the time-varying derivative of calibrated GPP from the measured values and the corresponding derivatives of Ta and VPD while having limited effects on the correlation between the calibrated GPP residual. In contrast to these two distinct calibration approaches, the combined calibration of both the SLOPE coefficient and GPP rate can concurrently reduce both coupling relationships.

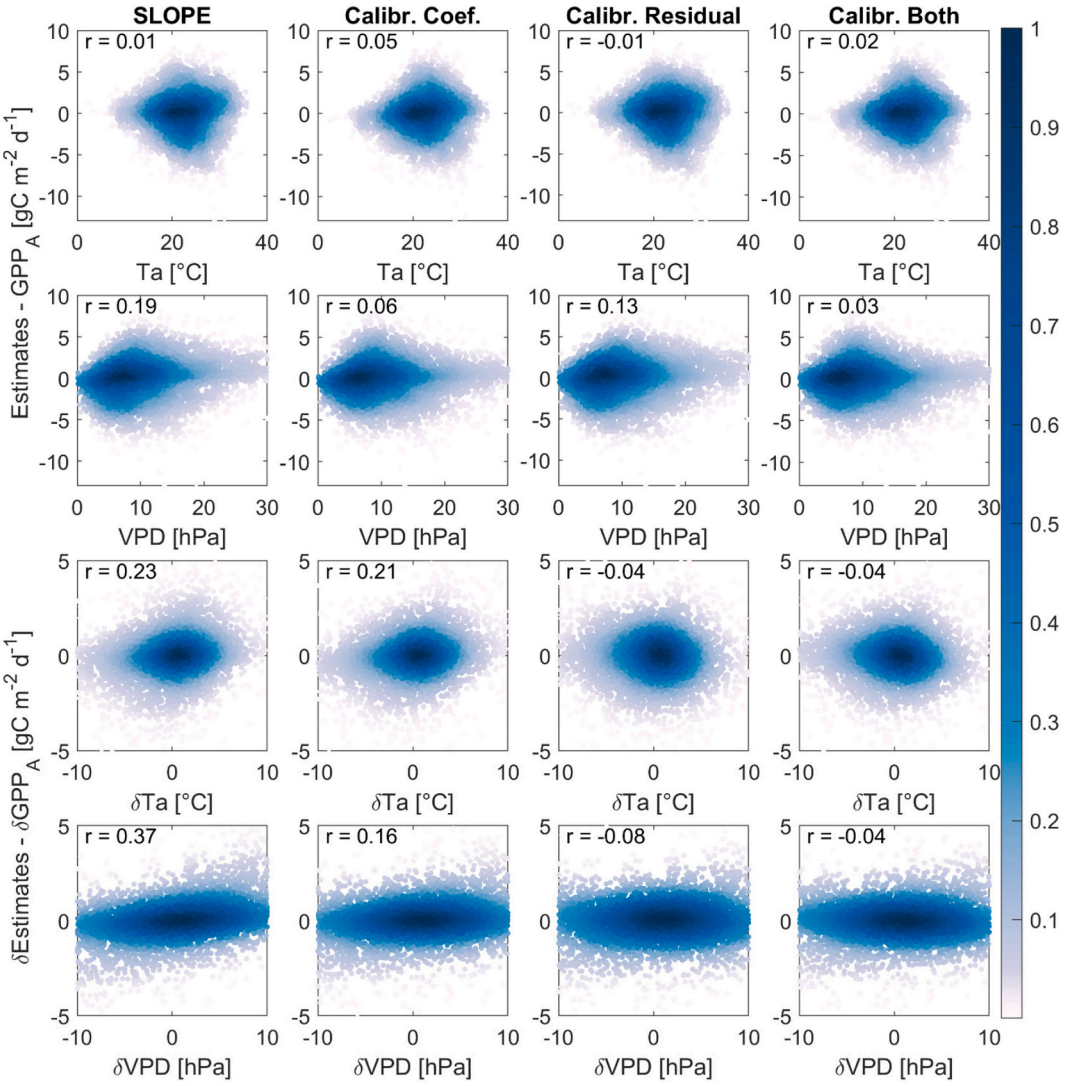

Fig. E1. Same as Fig. 5 but for grasslands.

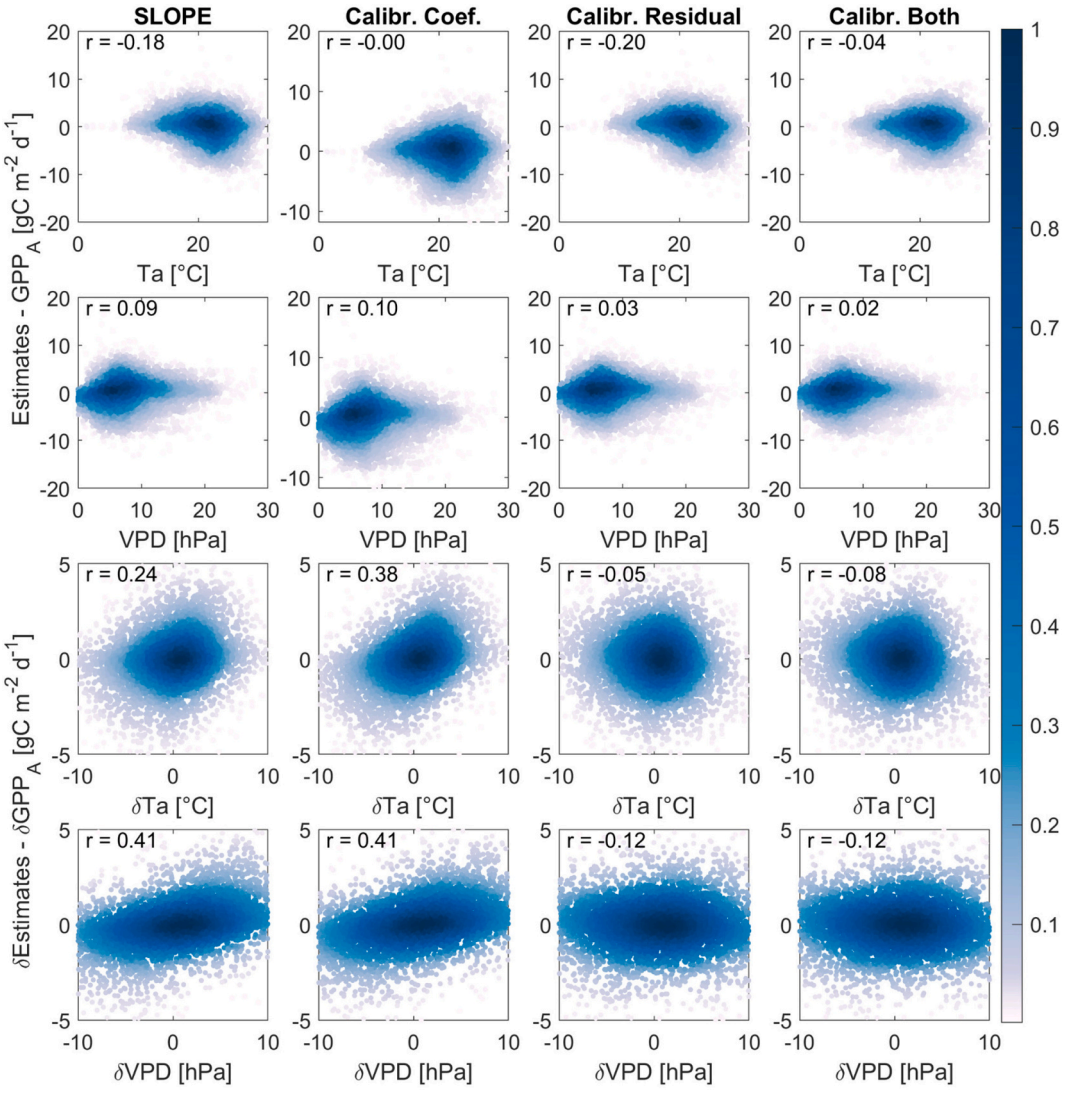

Fig. E2. Same as Fig. 5 but for C3 cropland.

Appendix F. Cross validation of ESLOPE along Ta and VPD gradients

As a complement to Fig. 6, we also generated plots for the bias and coefficient of determination (R^2) of SLOPE and ESLOPE GPP across the gradients of Ta and VPD in Figs. F1 & F2, which were based on leave-one-site-out cross-validation against measurements. The results in Fig. F1 show that ESLOPE GPP exhibited significantly lower bias compared to SLOPE GPP in most cases of Ta and VPD across different PFTs, particularly in situations characterized by extremely high VPD or low Ta. In grasslands, ESLOPE GPP consistently showed lower bias than SLOPE GPP. The reduction in ESLOPE GPP bias relative to SLOPE GPP was more pronounced as Ta and VPD increased, leading to an 82 % decrease in RMSE when VPD exceeded 30 hPa. In C3 croplands, SLOPE and ESLOPE models generally performed comparably in terms of bias, with ESLOPE GPP showing slightly lower bias than SLOPE GPP across most Ta gradients while slightly larger bias than SLOPE GPP along most VPD gradients. In the case where Ta was less than 15 °C, the reduction in ESLOPE GPP bias relative to SLOPE GPP was as high as 91 %. For C4 croplands, the bias of ESLOPE GPP was notably lower than that of SLOPE GPP along most Ta and VPD levels. The difference in bias between ESLOPE and SLOPE GPP was more prominent at relatively low and high Ta values. When Ta was below 15 °C, the reduction in ESLOPE GPP bias relative to SLOPE GPP bias exceeded 64 %.

Fig. F2 illustrates that ESLOPE GPP typically had a slightly higher temporal correlation with measurements than SLOPE GPP along most Ta and VPD gradients, especially for grasslands and C4 croplands. However, we also observed a notable decrease in the coefficient of determination of ESLOPE GPP against measurements compared to SLOPE GPP under extreme conditions such as when VPD was higher than 30 hPa in grasslands. This could be due to the fact that the uncertainties in VPD and Ta tended to increase in extreme cases, resulting in decreased temporal correlation between ESLOPE GPP and measurements.

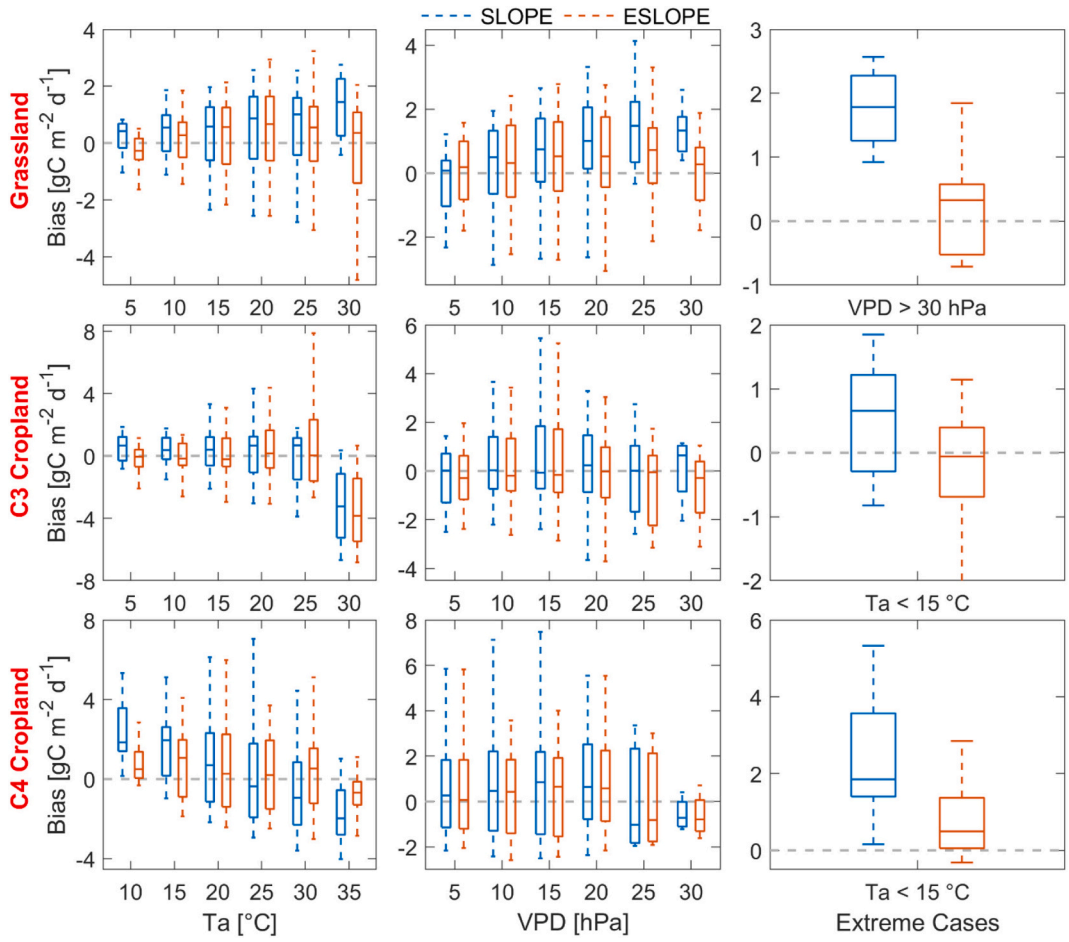

Fig. F1. Same as Fig. 6 but for bias.

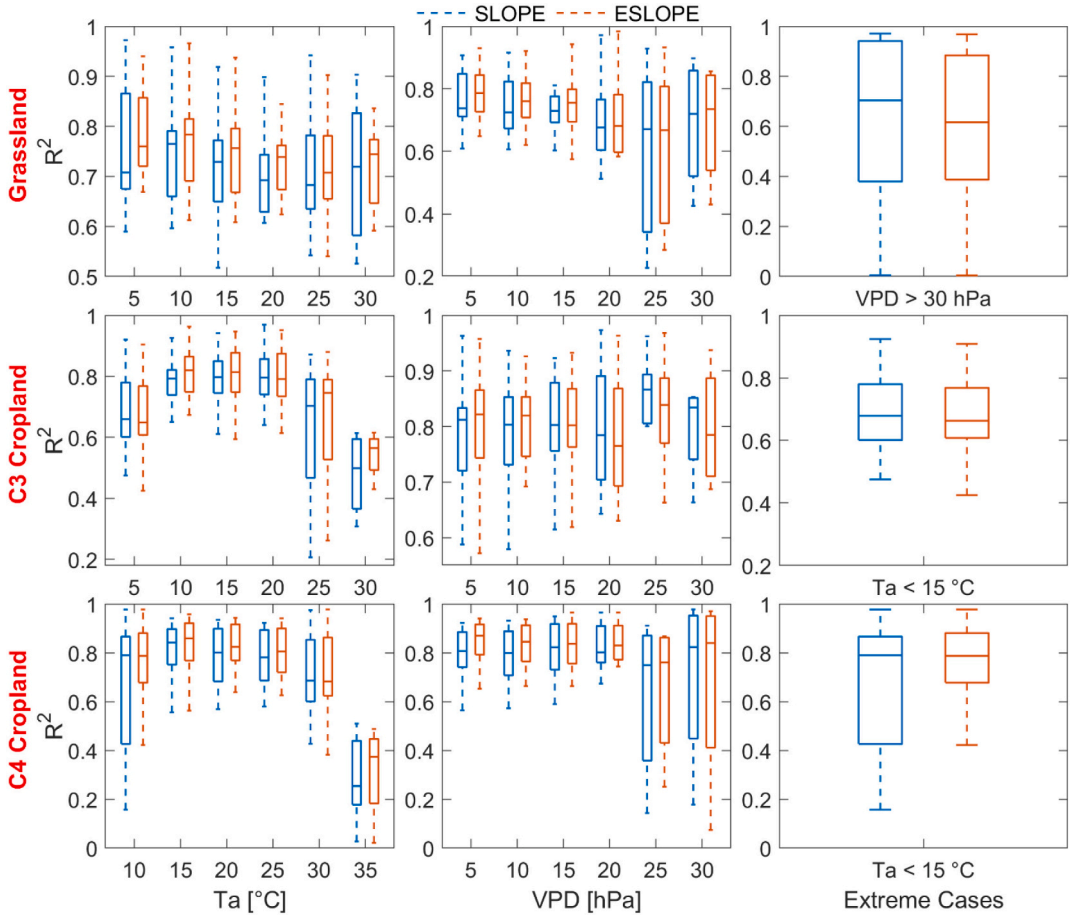

Fig. F2. Same as Fig. 6 but for the coefficient of determinant (R^2).

Appendix G. Time-series of ESLOPE GPP at C4 and C3 cropland sites

As complementary to Fig. 7, we plotted the SLOPE and ESLOPE GPP time series during the peak growing season of the grass in 2009 at the US-AR1 site (36.4°, −99.4°) and during the peak growing season of C3 crop in 2012 at the US-IB1 site (41.86°, −88.22°) (Figs. G1 & G2). For both sites, the results illustrate that ESLOPE and SLOPE GPP show a moderate to high temporal correlation with AmeriFlux measurements with the coefficient of determination greater than 0.7. When comparing ESLOPE and SLOPE GPP with EC measurements, we found that ESLOPE GPP notably outperformed SLOPE one with the coefficient of determination increased by more than 4.6 % and RMSE reduced by more than 3.2 % at both sites. Specifically, the improvements mainly happen when GPP has great variability within a short period of time, for example, during the period from 07/07/2009 and 07/14/2009 at the US-AR1 site and during the period from 07/21/2012 and 07/30/2012 at the US-IB1 site. This is because these severe daily variations in GPP were highly correlated with the huge fluctuations in Ta and VPD while incorporating Ta and VPD can effectively optimize SLOPE coefficients and thus GPP. On the other hand, we also observed considerable improvements in ESLOPE GPP relative to SLOPE one during the late growing season from 09/22/2009 to 09/30/2009 at the US-AR1 site and from 09/16/2012 to 09/30/2012 at the US-IB1 site. This is chiefly attributed to the fact that the decrease in GPP during the late growing season at both sites is synonymous with the reductions in Ta and VPD.

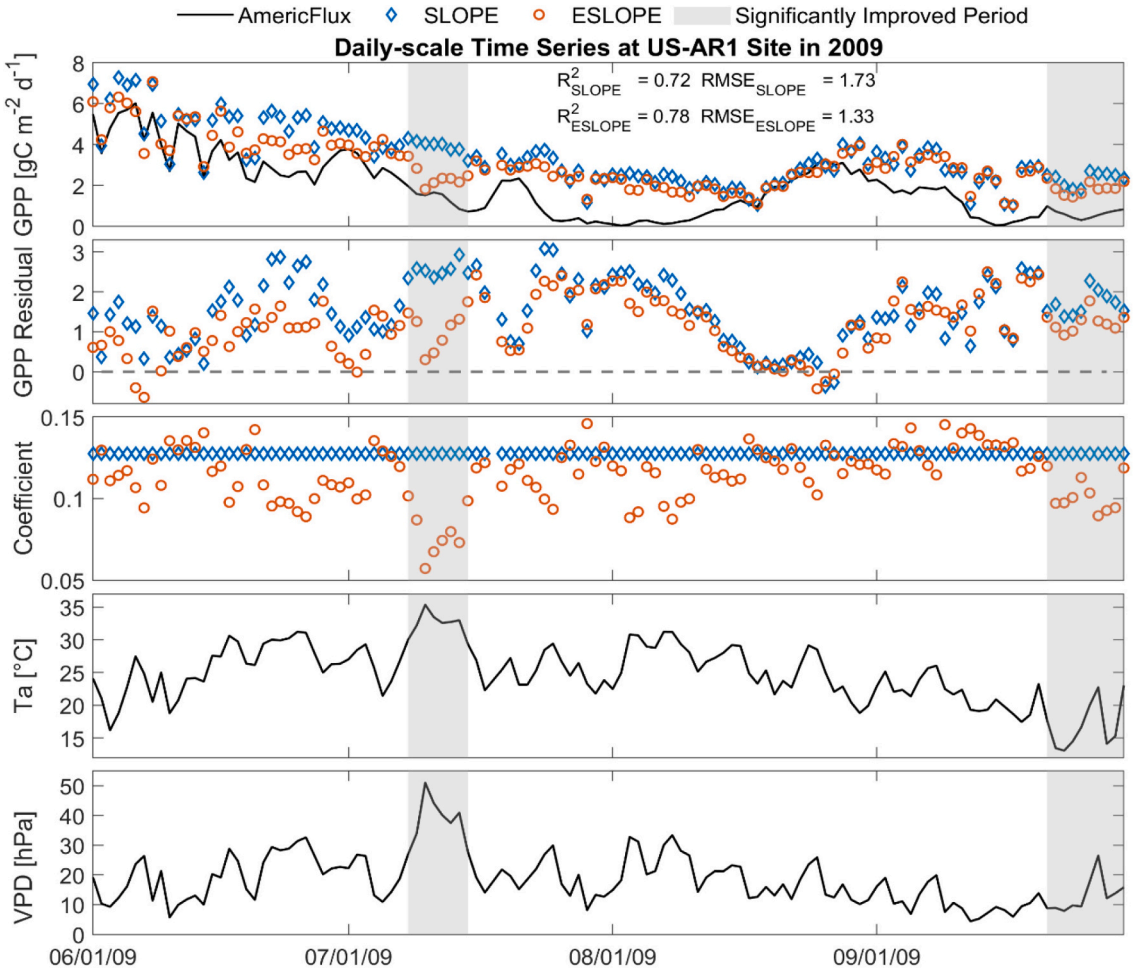

Fig. G1. Same as Fig. 7 but for the US-AR1 grassland site (36.4°, −99.4°) during the peak growing season of grass in 2009.

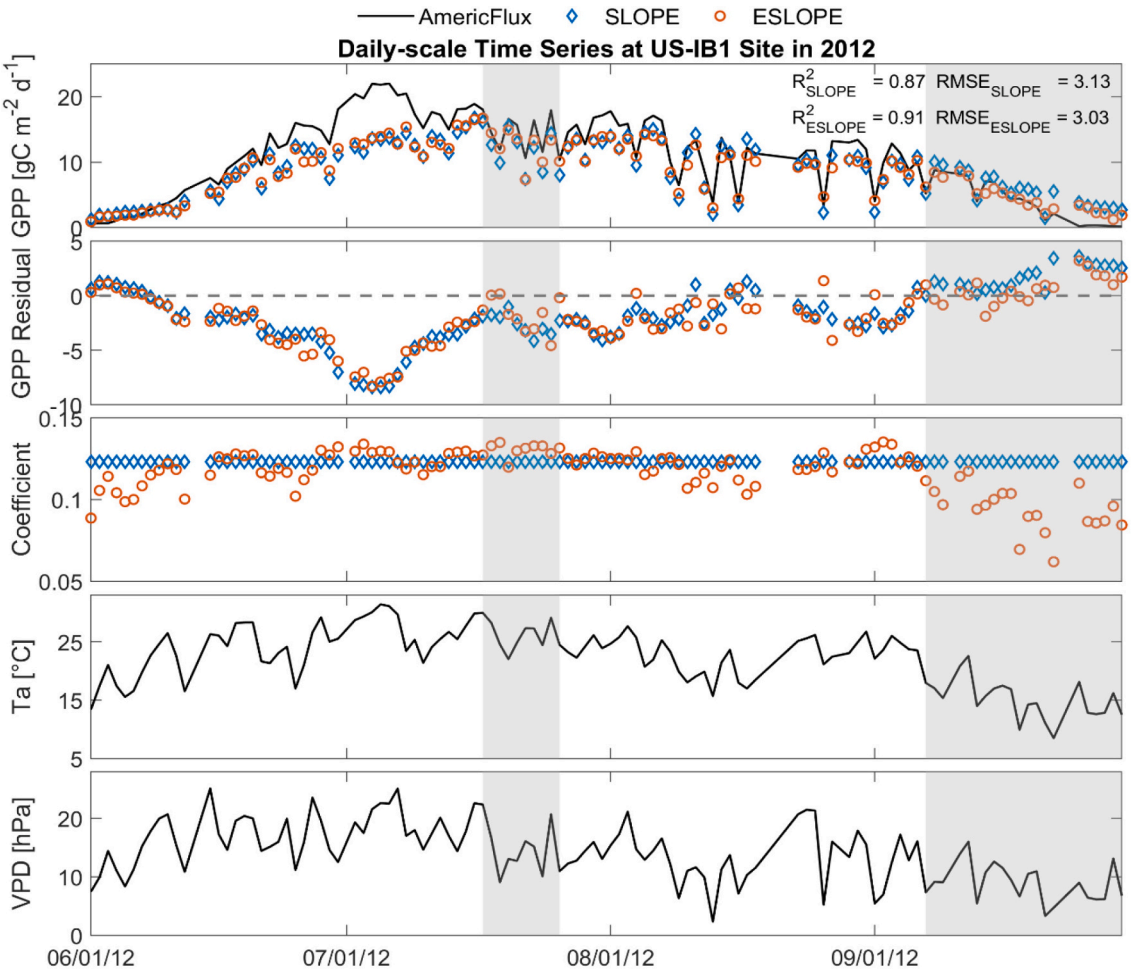

Fig. G2. Same as Fig. 7 but for the US-IB1 C3 cropland site (41.86°, −88.22°) during the peak growing season of C3 crop in 2012.

Appendix H. Effects of mixtures of C3 and C4 plants

To examine the effect of mixtures of C3 and C4 plants on our analysis, we reproduced Figs. 2 & 9 by only using pure satellite pixels without C4/C3 plant admixture. The results in Fig. H1 demonstrate that the relationship between SLOPE coefficients and environmental stress of Ta and VPD is quite consistent with that in Fig. 2. On the other hand, Fig. H2 illustrates that ESLOPE consistently outperforms most of other models, which is in line with that in Fig. 9. The consistent results indicate the robustness of our analysis and limited impact of EC representative issues on the results.

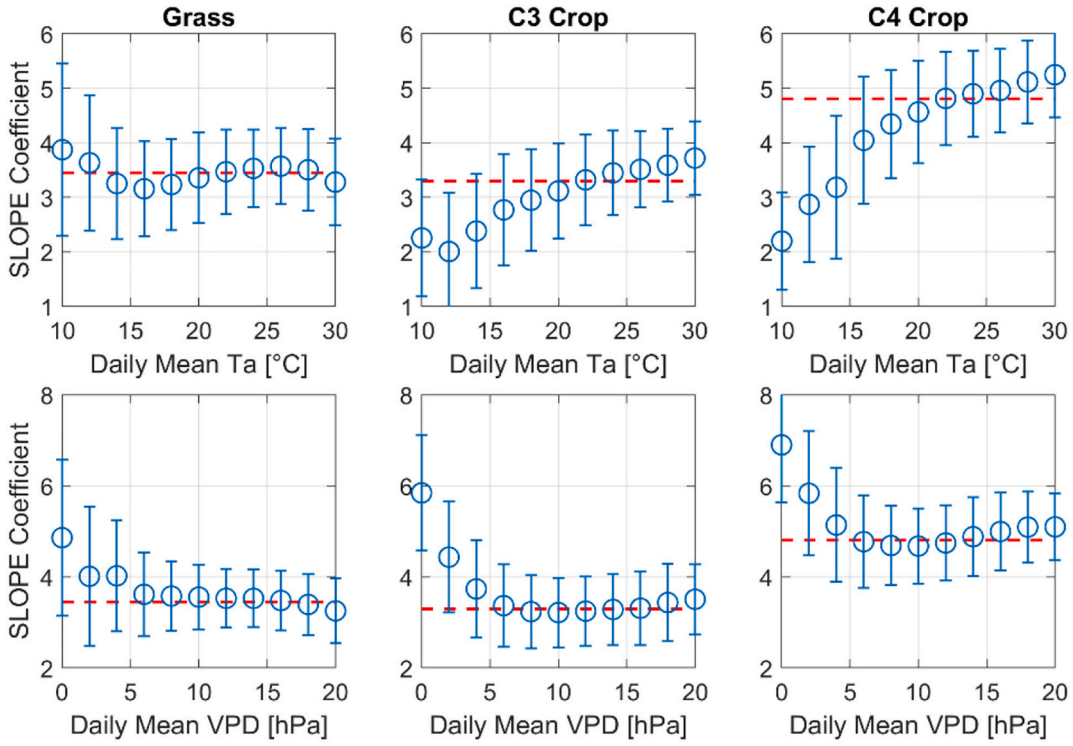

Fig. H1. Same as Fig. 2 but only for EC sites without mixed C3 and C4 plants.

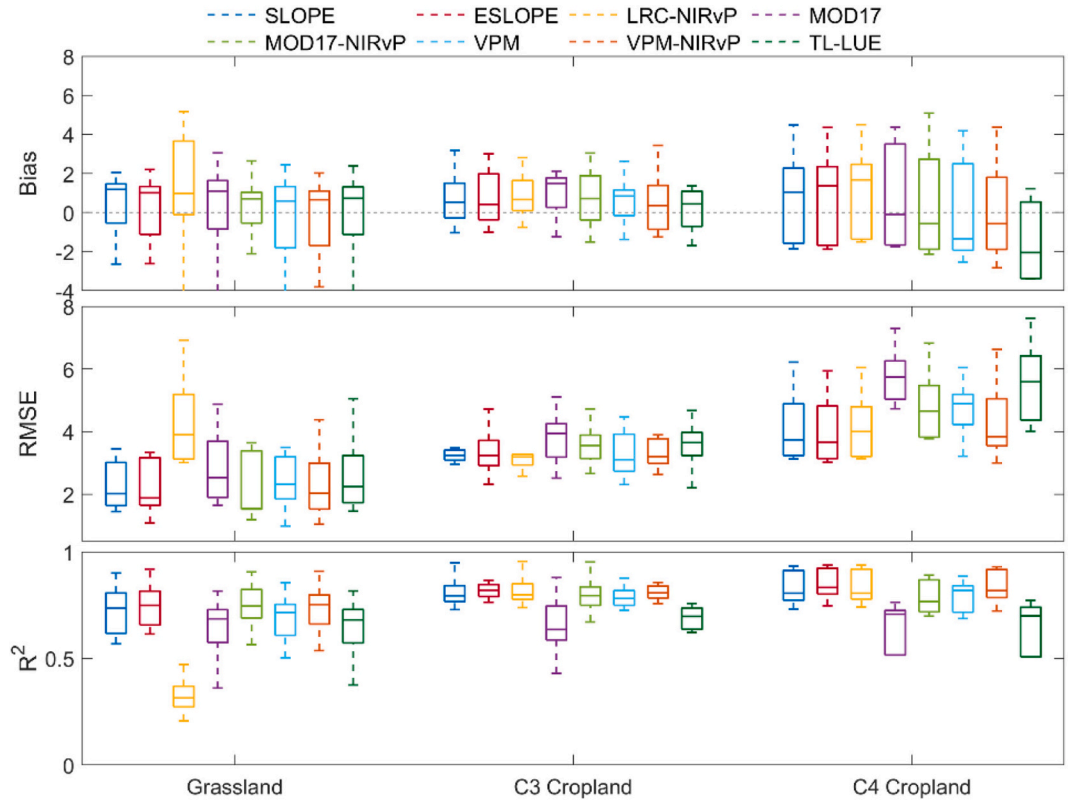

Fig. H2. Same as Fig. 9 but only for EC sites without mixed C3 and C4 plants.

Data availability

SLOPE datasets data were acquired from doi:https://doi.org/10.3334/ORNLDAAC/1786. AmeriFlux data are publicly available through https://ameriflux.lbl.gov/. PRISM data were downloaded from https://prism.oregonstate.edu/. MOD09A1 data are freely accessible via doi:https://doi.org/10.5067/MODIS/MOD09A1.061. MCD12C1 data were acquired from doi:https://doi.org/10.5067/MODIS/MCD12C1.061.

References

Ahlström, A., Raupach, M.R., Schurgers, G., Smith, B., Arneth, A., Jung, M., Reichstein, M., Canadell, J.G., Friedlingstein, P., Jain, A.K., Kato, E., 2015. The dominant role of semi-arid ecosystems in the trend and variability of the land CO2 sink. Science 348 (6237), 895–899.

Allen, R.G., Pereira, L.S., Raes, D., Smith, M., 1998. Crop evapotranspiration-guidelines for computing crop water requirements-FAO irrigation and drainage paper 56. Fao, Rome 300 (9), D05109.

Anav, A., Friedlingstein, P., Beer, C., Ciais, P., Harper, A., Jones, C., Murray-Tortarolo, G., Papale, D., Parazoo, N.C., Peylin, P., Piao, S., 2015. Spatiotemporal patterns of terrestrial gross primary production: a review. Rev. Geophys. 53 (3), 785–818.

Augustine, J.A., DeLuisi, J.J., Long, C.N., 2000. SURFRAD–A national surface radiation budget network for atmospheric research. Bull. Am. Meteorol. Soc. 81 (10), 2341–2358.

Badgley, G., Field, C.B., Berry, J.A., 2017. Canopy near-infrared reflectance and terrestrial photosynthesis. Sci. Adv. 3 (3), e1602244.

Badgley, G., Anderegg, L.D., Berry, J.A., Field, C.B., 2019. Terrestrial gross primary production: using NIRV to scale from site to globe. Glob. Chang. Biol. 25 (11), 3731–3740.

Baldocchi, D., Falge, E., Gu, L., Olson, R., Hollinger, D., Running, S., Anthoni, P., Bernhofer, C., Davis, K., Evans, R., Fuentes, J., 2001. FLUXNET: a new tool to study the temporal and spatial variability of ecosystem-scale carbon dioxide, water vapor, and energy flux densities. Bull. Am. Meteorol. Soc. 82 (11), 2415–2434.

Baldocchi, D.D., Ryu, Y., Dechant, B., Eichelmann, E., Hemes, K., Ma, S., et al., 2020. Outgoing near-infrared radiation from vegetation scales with canopy photosynthesis across a spectrum of function, structure, physiological capacity, and weather. J. Geophys. Res. Biogeosci. 125 (7), e2019JG005534.

Barcza, Z., Kern, A., Haszpra, L., Kljun, N., 2009. Spatial representativeness of tall tower eddy covariance measurements using remote sensing and footprint analysis. Agric. For. Meteorol. 149 (5), 795–807.

Baum, B.A., Menzel, W.P., Frey, R.A., Tobin, D.C., Holz, R.E., Ackerman, S.A., et al., 2012. MODIS cloud-top property refinements for collection 6. J. Appl. Meteorol. Climatol. 51 (6), 1145–1163.

Beck, H.E., Zimmermann, N.E., McVicar, T.R., Vergopolan, N., Berg, A., Wood, E.F., 2018. Present and future Köppen-Geiger climate classification maps at 1-km resolution. Sci. Data 5 (1), 1–12.

Beer, C., Reichstein, M., Tomelleri, E., Ciais, P., Jung, M., Carvalhais, N., Rödenbeck, C., Arain, M.A., Baldocchi, D., Bonan, G.B., Bondeau, A., 2010. Terrestrial gross carbon dioxide uptake: global distribution and covariation with climate. Science 329 (5993), 834–838.

Bernacchi, C.J., Portis, A.R., Nakano, H., Von Caemmerer, S., Long, S.P., 2002. Temperature response of mesophyll conductance. Implications for the determination of rubisco enzyme kinetics and for limitations to photosynthesis in vivo. Plant Physiol. 130 (4), 1992–1998.

Bewick, V., Cheek, L., Ball, J., 2004. Statistics review 9: one-way analysis of variance. J. Crit. Care 8, 1–7.

Boryan, C., Yang, Z., Mueller, R., Craig, M., 2011. Monitoring US agriculture: the US department of agriculture, national agricultural statistics service, cropland data layer program. Geocarto Int. 26 (5), 341–358.

Bristow, K.L., Campbell, G.S., 1984. On the relationship between incoming solar radiation and daily maximum and minimum temperature. Agric. For. Meteorol. 31 (2), 159–166.

Chang, L., Gao, G., Jin, S., He, X., Xiao, R., Guo, L., 2014. Calibration and evaluation of precipitable water vapor from MODIS infrared observations at night. IEEE Trans. Geosci. Remote Sens. 53 (5), 2612–2620.

Chen, J.M., Black, T.A., 1992. Defining leaf area index for non-flat leaves. Plant Cell Environ. 15 (4), 421–429.

Chen, J.M., Liu, J., Cihlar, J., Goulden, M.L., 1999. Daily canopy photosynthesis model through temporal and spatial scaling for remote sensing applications. Ecol. Model. 124 (2–3), 99–119.

Chen, B., Coops, N.C., Fu, D., Margolis, H.A., Amiro, B.D., Black, T.A., et al., 2012. Characterizing spatial representativeness of flux tower eddy-covariance measurements across the Canadian carbon program network using remote sensing and footprint analysis. Remote Sens. Environ. 124, 742–755.

Chen, R., Yin, G., Liu, G., Yang, Y., Wang, C., Xie, Q., et al., 2023. Correction of illumination effects on seasonal divergent NIRv photosynthetic phenology. Agric. For. Meteorol. 339, 109542.

Chu, H., Luo, X., Ouyang, Z., Chan, W.S., Dengel, S., Biraud, S.C., Torn, M.S., Metzger, S., Kumar, J., Arain, M.A., Arkebauer, T.J., 2021. Representativeness of Eddy-covariance flux footprints for areas surrounding AmeriFlux sites. Agric. For. Meteorol. 301, 108350.

Corbosiero, K.L., Dickinson, M.J., Bosart, L.F., 2009. The contribution of eastern North Pacific tropical cyclones to the rainfall climatology of the Southwest United States. Mon. Weather Rev. 137 (8), 2415–2435.

Cui, T., Wang, Y., Sun, R., Qiao, C., Fan, W., Jiang, G., et al., 2016. Estimating vegetation primary production in the Heihe River basin of China with multi-source and multi-scale data. PLoS One 11 (4), e0153971.

Daly, C., Taylor, G.H., Gibson, W.P., Parzybok, T.W., Johnson, G.L., Pasteris, P.A., 2000. High-quality spatial climate data sets for the United States and beyond. Trans ASAE 43 (6), 1957.

Daly, C., Halbleib, M., Smith, J.I., Gibson, W.P., Doggett, M.K., Taylor, G.H., et al., 2008. Physiographically sensitive mapping of climatological temperature and precipitation across the conterminous United States. Int. J. Climatol. 28 (15), 2031–2064.

de Almeida, C.T., Delgado, R.C., Galvao, L.S., Ramos, M.C., 2018. Improvements of the MODIS gross primary productivity model based on a comprehensive uncertainty assessment over the Brazilian Amazonia. ISPRS J. Photogramm. Remote Sens. 145, 268–283.

Dechant, B., Ryu, Y., Badgley, G., Zeng, Y., Berry, J.A., Zhang, Y., et al., 2020. Canopy structure explains the relationship between photosynthesis and sun-induced chlorophyll fluorescence in crops. Remote Sens. Environ. 241, 111733.

Dechant, B., Ryu, Y., Badgley, G., Köhler, P., Rascher, U., Migliavacca, M., et al., 2022. NIRVP: a robust structural proxy for sun-induced chlorophyll fluorescence and photosynthesis across scales. Remote Sens. Environ. 268, 112763.

Dee, D.P., Uppala, S.M., Simmons, A.J., Berrisford, P., Poli, P., Kobayashi, S., et al., 2011. The ERA-interim reanalysis: configuration and performance of the data assimilation system. Q. J. R. Meteorol. Soc. 137 (656), 553–597.

Doughty, R., Xiao, X., Köhler, P., Frankenberg, C., Qin, Y., Wu, X., et al., 2021. Global-scale consistency of spaceborne vegetation indices, chlorophyll fluorescence, and photosynthesis. J. Geophys. Res. Biogeosci. 126 (6), e2020JG006136.

Drummond, M.A., Auch, R.F., Karstensen, K.A., Sayler, K.L., Taylor, J.L., Loveland, T.R., 2012. Land change variability and human–environment dynamics in the United States Great Plains. Land Use Policy 29 (3), 710–723.

Farquhar, G.D., Von Caemmerer, S., 1982. Modelling of photosynthetic response to environmental conditions. In: Physiological Plant Ecology II: Water Relations and Carbon Assimilation. Springer Berlin Heidelberg, Berlin, Heidelberg, pp. 549–587.

Frankenberg, C., Berry, J., 2018. 3.10 solar induced chlorophyll fluorescence: origins, relation to photosynthesis and retrieval. Comp. Remote Sens. 3, 143–162.

Frankenberg, C., Fisher, J.B., Worden, J., Badgley, G., Saatchi, S.S., Lee, J.E., et al., 2011. New global observations of the terrestrial carbon cycle from GOSAT: patterns of plant fluorescence with gross primary productivity. Geophys. Res. Lett. 38 (17).

Friedl, M., Sulla-Menashe, D., 2015. MCD12C1 MODIS/Terra+Aqua Land Cover Type Yearly L3 Global 0.05Deg CMG V006 [Data set]. NASA EOSDIS Land Processes DAAC.

Friedman, J.H., 1991. Multivariate adaptive regression splines. Ann. Stat. 19 (1), 1–67.

Fu, Z., Ciais, P., Bastos, A., Stoy, P.C., Yang, H., Green, J.K., Wang, B., Yu, K., Huang, Y., Knohl, A., 2020. Sensitivity of gross primary productivity to climatic drivers during the summer drought of 2018 in Europe. Philos. Trans. R. Soc. B 375 (1810), 20190747.

Gao, L., Sadeghi, M., Ebtehaj, A., 2020. Microwave retrievals of soil moisture and vegetation optical depth with improved resolution using a combined constrained inversion algorithm: Application for SMAP satellite. Remote. Sens. Environ. 239, 111662.

Gao, Y., Yu, G., Yan, H., Zhu, X., Li, S., Wang, Q., et al., 2014. A MODIS-based photosynthetic capacity model to estimate gross primary production in northern China and the Tibetan plateau. Remote Sens. Environ. 148, 108–118.

Gao, L., Ebtehaj, A., Chaubell, M.J., Sadeghi, M., Li, X., Wigneron, J.P., 2021. Reappraisal of SMAP inversion algorithms for soil moisture and vegetation optical depth. Remote. Sens. Environ. 264, 112627.

Gao, L., Gao, Q., Zhang, H., Li, X., Chaubell, M.J., Ebtehaj, A., Shen, L., Wigneron, J.P., 2022. A deep neural network based SMAP soil moisture product. Remote. Sens. Environ. 277, 113059.

Gao, L., Guan, K., He, L., Jiang, C., Wu, X., Lu, X., Ainsworth, E.A., 2024. Tropospheric ozone pollution increases the sensitivity of plant production to vapor pressure deficit across diverse ecosystems in the northern hemisphere. Sci. Total Environ. 175748.

Gentine, P., Alemohammad, S.H., 2018. Reconstructed solar-induced fluorescence: A machine learning vegetation product based on MODIS surface reflectance to reproduce GOME-2 solar-induced fluorescence. Geophys. Res. Lett. 45 (7), 3136–3146.

Goldberger, J., Hinton, G.E., Roweis, S., Salakhutdinov, R.R., 2004. Neighbourhood components analysis. Adv. Neural Inf. Proces. Syst. 17.

Green, T.R., Kipka, H., David, O., McMaster, G.S., 2018. Where is the USA Corn Belt, and how is it changing? Sci. Total Environ. 618, 1613–1618.

Guan, K., Berry, J.A., Zhang, Y., Joiner, J., Guanter, L., Badgley, G., Lobell, D.B., 2016. Improving the monitoring of crop productivity using spaceborne solar-induced fluorescence. Glob. Chang. Biol. 22 (2), 716–726.

Guanter, L., Alonso, L., Gómez-Chova, L., Amorós-López, J., Vila, J., Moreno, J., 2007. Estimation of solar-induced vegetation fluorescence from space measurements. Geophys. Res. Lett. 34 (8).

Guanter, L., Frankenberg, C., Dudhia, A., Lewis, P.E., Gómez-Dans, J., Kuze, A., et al., 2012. Retrieval and global assessment of terrestrial chlorophyll fluorescence from GOSAT space measurements. Remote Sens. Environ. 121, 236–251.

Guanter, L., Zhang, Y., Jung, M., Joiner, J., Voigt, M., Berry, J.A., et al., 2014. Global and time-resolved monitoring of crop photosynthesis with chlorophyll fluorescence. Proc. Natl. Acad. Sci. 111 (14), E1327–E1333.

Hatfield, J., 2012. Agriculture in the Midwest. In: US National Climate Assessment Midwest Technical Input Report, pp. 1–8.
He, M., Ju, W., Zhou, Y., Chen, J., He, H., Wang, S., et al., 2013. Development of a two-leaf light use efficiency model for improving the calculation of terrestrial gross primary productivity. Agric. For. Meteorol. 173, 28–39.
He, M., Kimball, J.S., Running, S., Ballantyne, A., Guan, K., Huemmrich, F., 2016. Satellite detection of soil moisture related water stress impacts on ecosystem productivity using the MODIS-based photochemical reflectance index. Remote Sens. Environ. 186, 173–183.
He, L., Magney, T., Dutta, D., Yin, Y., Köhler, P., Grossmann, K., et al., 2020. From the ground to space: using solar-induced chlorophyll fluorescence to estimate crop productivity. Geophys. Res. Lett. 47 (7), e2020GL087474.
He, W., Ju, W., Jiang, F., Parazoo, N., Gentine, P., Wu, X., Zhang, C., Zhu, J., Viovy, N., Jain, A.K., 2021. Peak growing season patterns and climate extremes-driven responses of gross primary production estimated by satellite and process based models over North America. Agric. For. Meteorol. 298, 108292.
Heinemann, J.A., Massaro, M., Coray, D.S., Agapito-Tenfen, S.Z., Wen, J.D., 2014. Sustainability and innovation in staple crop production in the US Midwest. Int. J. Agric. Sustain. 12 (1), 71–88.
Hikosaka, K., Hirose, T., 1997. Leaf angle as a strategy for light competition: optimal and evolutionarily stable light-extinction coefficient within a leaf canopy. Ecoscience 4 (4), 501–507.
Homer, C., Huang, C., Yang, L., Wylie, B., Coan, M., 2004. Development of a 2001 national land-cover database for the United States. Photogramm. Eng. Remote. Sens. 70 (7), 829–840.
Huang, X., Xiao, J., Ma, M., 2019. Evaluating the performance of satellite-derived vegetation indices for estimating gross primary productivity using FLUXNET observations across the globe. Remote Sens. 11 (15), 1823.
Huete, A.R., Liu, H.Q., Batchily, K.V., Van Leeuwen, W.J.D.A., 1997. A comparison of vegetation indices over a global set of TM images for EOS-MODIS. Remote Sens. Environ. 59 (3), 440–451.
Huete, A., Didan, K., Miura, T., Rodriguez, E.P., Gao, X., Ferreira, L.G., 2002. Overview of the radiometric and biophysical performance of the MODIS vegetation indices. Remote Sens. Environ. 83 (1–2), 195–213.
Jiang, C., Fang, H., 2019. GSV: a general model for hyperspectral soil reflectance simulation. Int. J. Appl. Earth Obs. Geoinf. 83, 101932.
Jiang, C., Guan, K., 2020. MODIS-based GPP, PAR, fC4, and SANIRv estimates from SLOPE for CONUS, 2000-2019. ORNL DAAC, Oak Ridge, Tennessee, USA. https://doi.org/10.3334/ORNLDAAC/1786.
Jiang, C., Guan, K., Wu, G., Peng, B., Wang, S., 2021. A daily, 250 m and real-time gross primary productivity product (2000–present) covering the contiguous United States. Earth Syst. Sci. Data 13 (2), 281–298.
Johnson, G.L., Daly, C., Taylor, G.H., Hanson, C.L., 2000. Spatial variability and interpolation of stochastic weather simulation model parameters. J. Appl. Meteorol. Climatol. 39 (6), 778–796.
Joiner, J., Yoshida, Y., Vasilkov, A.P., Schaefer, K., Jung, M., Guanter, L., et al., 2014. The seasonal cycle of satellite chlorophyll fluorescence observations and its relationship to vegetation phenology and ecosystem atmosphere carbon exchange. Remote Sens. Environ. 152, 375–391.
Khan, A.M., Stoy, P.C., Joiner, J., Baldocchi, D., Verfaillie, J., Chen, M., Otkin, J.A., 2022. The diurnal dynamics of gross primary productivity using observations from the advanced baseline imager on the geostationary operational environmental satellite-R series at an oak savanna ecosystem. J. Geophys. Res. Biogeosci. 127 (3), e2021JG006701.
Klemm, T., Briske, D.D., 2021. Retrospective assessment of beef cow numbers to climate variability throughout the US Great Plains. Rangel. Ecol. Manag. 78, 273–280.
Kobrick, M., Crippen, R., 2013. SRTMGL1: NASA shuttle radar topography Mission Global 1 arc second V003. In: NASA EOSDIS Land Processes DAAC.
Kong, J., Ryu, Y., Liu, J., Dechant, B., Rey-Sanchez, C., Shortt, R., et al., 2022. Matching high resolution satellite data and flux tower footprints improves their agreement in photosynthesis estimates. Agric. For. Meteorol. 316, 108878.
Kumar, J., Hoffman, F.M., Hargrove, W.W., Collier, N., 2016. Understanding the representativeness of FLUXNET for upscaling carbon flux from eddy covariance measurements. Earth Syst. Sci. Data Discuss. 1–25.
Landsberg, J.J., Waring, R.H., 1997. A generalised model of forest productivity using simplified concepts of radiation-use efficiency, carbon balance and partitioning. Forest Ecol. Manag. 95 (3), 209–228.
Lasslop, G., Reichstein, M., Papale, D., Richardson, A.D., Arneth, A., Barr, A., et al., 2010. Separation of net ecosystem exchange into assimilation and respiration using a light response curve approach: critical issues and global evaluation. Glob. Chang. Biol. 16 (1), 187–208.
Law, B.E., Falge, E., Gu, L.V., Baldocchi, D.D., Bakwin, P., Berbigier, P., Davis, K., Dolman, A.J., Falk, M., Fuentes, J.D., Goldstein, A., 2002. Environmental controls over carbon dioxide and water vapor exchange of terrestrial vegetation. Agric. For. Meteorol. 113 (1–4), 97–120.
Leuning, R., 1995. A critical appraisal of a combined stomatal-photosynthesis model for C3 plants. Plant Cell Environ. 18 (4), 339–355.
Leuning, R., Cleugh, H.A., Zegelin, S.J., Hughes, D., 2005. Carbon and water fluxes over a temperate Eucalyptus forest and a tropical wet/dry savanna in Australia: measurements and comparison with MODIS remote sensing estimates. Agric. For. Meteorol. 129 (3–4), 151–173.
Leverenz, J.W., Jarvis, P.G., 1980. Photosynthesis in Sitka spruce (Picea sitchensis (bong.) Carr.). IX. The relative contribution made by needles at various positions on the shoot. J. Appl. Ecol. 59–68.
Li, X., Xiao, J., 2019. A global, 0.05-degree product of solar-induced chlorophyll fluorescence derived from OCO-2, MODIS, and reanalysis data. Remote Sens. 11 (5), 517.
Liang, S., Wang, J. (Eds.), 2019. Advanced Remote Sensing: Terrestrial Information Extraction and Applications. Academic Press.
Liaw, A., Wiener, M., 2002. Classification and regression by randomForest. R News 2 (3), 18–22.
Liu, L., Gudmundsson, L., Hauser, M., Qin, D., Li, S., Seneviratne, S.I., 2020a. Soil moisture dominates dryness stress on ecosystem production globally. Nat. Commun. 11 (1), 4892.
Liu, Y., Kumar, M., Katul, G.G., Feng, X., Konings, A.G., 2020b. Plant hydraulics accentuates the effect of atmospheric moisture stress on transpiration. Nat. Clim. Chang. 10 (7), 691–695.
Liu, L., Liu, X., Chen, J., Du, S., Ma, Y., Qian, X., et al., 2020c. Estimating maize GPP using near-infrared radiance of vegetation. Sci. Remote Sens. 2, 100009.
Mengistu, A.G., Mengistu Tsidu, G., Koren, G., Kooreman, M.L., Boersma, K.F., Tagesson, T., et al., 2021. Sun-induced fluorescence and near-infrared reflectance of vegetation track the seasonal dynamics of gross primary production over Africa. Biogeosciences 18 (9), 2843–2857.
Mercado, L.M., Bellouin, N., Sitch, S., Boucher, O., Huntingford, C., Wild, M., Cox, P.M., 2009. Impact of changes in diffuse radiation on the global land carbon sink. Nature 458 (7241), 1014–1017.
Miao, G., Guan, K., Yang, X., Bernacchi, C.J., Berry, J.A., DeLucia, E.H., et al., 2018. Sun-induced chlorophyll fluorescence, photosynthesis, and light use efficiency of a soybean field from seasonally continuous measurements. J. Geophys. Res. Biogeosci. 123 (2), 610–623.
Mohammed, G.H., Colombo, R., Middleton, E.M., Rascher, U., van der Tol, C., Nedbal, L., et al., 2019. Remote sensing of solar-induced chlorophyll fluorescence (SIF) in vegetation: 50 years of progress. Remote Sens. Environ. 231, 111177.
Montandon, L.M., Small, E.E., 2008. The impact of soil reflectance on the quantification of the green vegetation fraction from NDVI. Remote Sens. Environ. 112 (4), 1835–1845.
Monteith, J.L., 1972. Solar radiation and productivity in tropical ecosystems. J. Appl. Ecol. 9 (3), 747–766.
Monteith, J.L., 1977. Climate and the efficiency of crop production in Britain. Phil. Trans. Roy. Soc. Lond. B 281 (980), 277–294.
Moore, C.E., Meacham-Hensold, K., Lemonnier, P., Slattery, R.A., Benjamin, C., Bernacchi, C.J., Lawson, T., Cavanagh, A.P., 2021. The effect of increasing temperature on crop photosynthesis: from enzymes to ecosystems. J. Exp. Bot. 72 (8), 2822–2844.
Norman, J.M., 1982. Simulation of microclimates. In: Biometeorology in Integrated Pest Management, 65.
Novick, K.A., Ficklin, D.L., Stoy, P.C., Williams, C.A., Bohrer, G., Oishi, A.C., Papuga, S. A., Blanken, P.D., Noormets, A., Sulman, B.N., 2016. The increasing importance of atmospheric demand for ecosystem water and carbon fluxes. Nat. Clim. Chang. 6 (11), 1023–1027.
Oliphant, A.J., Dragoni, D., Deng, B., Grimmond, C.S.B., Schmid, H.P., Scott, S.L., 2011. The role of sky conditions on gross primary production in a mixed deciduous forest. Agric. For. Meteorol. 151 (7), 781–791.
Pabon-Moreno, D.E., Migliavacca, M., Reichstein, M., Mahecha, M.D., 2022. On the potential of Sentinel-2 for estimating gross primary production. IEEE Trans. Geosci. Remote Sens. 60, 1–12.
Pastorello, G., 2019. ONEFlux: Open Network-Enabled Flux processing pipeline. In: AmeriFlux Management Project. European Ecosystem Fluxes Database, ICOS Ecosystem Thematic Center.
Pastorello, G., Trotta, C., Canfora, E., Chu, H., Christianson, D., Cheah, Y.W., et al., 2020. The FLUXNET2015 dataset and the ONEFlux processing pipeline for eddy covariance data. Sci. Data 7 (1), 1–27.
Pei, Y., Dong, J., Zhang, Y., Yuan, W., Doughty, R., Yang, J., et al., 2022. Evolution of light use efficiency models: improvement, uncertainties, and implications. Agric. For. Meteorol. 317, 108905.
Piao, S., Fang, J., Ciais, P., Peylin, P., Huang, Y., Sitch, S., Wang, T., 2009. The carbon balance of terrestrial ecosystems in China. Nature 458 (7241), 1009–1013.
Potter, C.S., Randerson, J.T., Field, C.B., Matson, P.A., Vitousek, P.M., Mooney, H.A., Klooster, S.A., 1993. Terrestrial ecosystem production: a process model based on global satellite and surface data. Glob. Biogeochem. Cycles 7 (4), 811–841.
Prince, S.D., Goward, S.N., 1995. Global primary production: a remote sensing approach. J. Biogeogr. 815–835.
Raich, J.W., Rastetter, E.B., Melillo, J.M., Kicklighter, D.W., Steudler, P.A., Peterson, B. J., et al., 1991. Potential net primary productivity in South America: application of a global model. Ecol. Appl. 1 (4), 399–429.
Reichstein, M., Falge, E., Baldocchi, D., Papale, D., Aubinet, M., Berbigier, P., et al., 2005. On the separation of net ecosystem exchange into assimilation and ecosystem respiration: review and improved algorithm. Glob. Chang. Biol. 11 (9), 1424–1439.
Reichstein, M., Stoy, P.C., Desai, A.R., Lasslop, G., Richardson, A.D., 2012. Partitioning of net fluxes. In: Eddy Covariance: A Practical Guide to Measurement and Data Analysis, pp. 263–289.
Remer, L.A., Mattoo, S., Levy, R.C., Munchak, L.A., 2013. MODIS 3 km aerosol product: algorithm and global perspective. Atmos. Meas. Tech. 6 (7), 1829–1844.
Rigden, A., Mueller, N., Holbrook, N., Pillai, N., Huybers, P., 2020. Combined influence of soil moisture and atmospheric evaporative demand is important for accurately predicting US maize yields. Nat. Food 1 (2), 127–133.
Roderick, M.L., Farquhar, G.D., Berry, S.L., Noble, I.R., 2001. On the direct effect of clouds and atmospheric particles on the productivity and structure of vegetation. Oecologia 129, 21–30.

Román, M.O., Schaaf, C.B., Woodcock, C.E., Strahler, A.H., Yang, X., Braswell, R.H., et al., 2009. The MODIS (Collection V005) BRDF/albedo product: Assessment of spatial representativeness over forested landscapes. Remote Sens. Environ. 113 (11), 2476–2498.
Running, S.W., 2012. A measurable planetary boundary for the biosphere. Science 337 (6101), 1458–1459.
Running, S.W., Nemani, R.R., 1988. Relating seasonal patterns of the AVHRR vegetation index to simulated photosynthesis and transpiration of forests in different climates. Remote Sens. Environ. 24 (2), 347–367.
Running, S.W., Zhao, M., 2019. User's guide daily GPP and annual NPP (MOD17A2H/A3H) and year-end gap-filled (MOD17A2HGF/A3HGF) products NASA Earth Observing System MODIS Land Algorithm (For Collection 6). Process. DAAC 490, 1–37.
Running, S.W., Nemani, R., Glassy, J.M., Thornton, P.E., 1999. MODIS Daily Photosynthesis (PSN) and Annual Net Primary Production (NPP) Product (MOD17) Algorithm Theoretical Basis Document.
Running, S.W., Nemani, R.R., Heinsch, F.A., Zhao, M., Reeves, M., Hashimoto, H., 2004. A continuous satellite-derived measure of global terrestrial primary production. Bioscience 54 (6), 547–560.
Ryu, Y., Berry, J.A., Baldocchi, D.D., 2019. What is global photosynthesis? History, uncertainties and opportunities. Remote Sens. Environ. 223, 95–114.
Schaaf, C.B., Gao, F., Strahler, A.H., Lucht, W., Li, X., Tsang, T., et al., 2002. First operational BRDF, albedo nadir reflectance products from MODIS. Remote Sens. Environ. 83 (1–2), 135–148.
Seemann, S.W., Borbas, E.E., Li, J., Menzel, W.P., Gumley, L.E., 2006. MODIS Atmospheric Profile Retrieval Algorithm Theoretical Basis Document. Cooperative Institute for Meteorological Satellite Studies, University of Wisconsin-Madison, Madison, WI. Version, 6.
Stearns, F.W., Carlson, C.A., 1960. Correlations between soil-moisture depletion, solar radiation, and other environmental factors. J. Geophys. Res. 65 (11), 3727–3732.
Stocker, B.D., Zscheischler, J., Keenan, T.F., Prentice, I.C., Peñuelas, J., Seneviratne, S.I., 2018. Quantifying soil moisture impacts on light use efficiency across biomes. New Phytol. 218 (4), 1430–1449.
Stocker, B.D., Zscheischler, J., Keenan, T.F., Prentice, I.C., Seneviratne, S.I., Peñuelas, J., 2019. Drought impacts on terrestrial primary production underestimated by satellite monitoring. Nat. Geosci. 12 (4), 264–270.
Sulman, B.N., Roman, D.T., Yi, K., Wang, L., Phillips, R.P., Novick, K.A., 2016. High atmospheric demand for water can limit forest carbon uptake and transpiration as severely as dry soil. Geophys. Res. Lett. 43 (18), 9686–9695.
Sun, Y., Wen, J., Gu, L., Joiner, J., Chang, C.Y., van der Tol, C., et al., 2023. From remotely-sensed solar-induced chlorophyll fluorescence to ecosystem structure, function, and service: Part II—Harnessing data. Glob. Chang. Biol. 29 (11), 2893–2925.
Tibshirani, R., 1996. Regression shrinkage and selection via the lasso. J. Roy. Stat. Soc. Ser. B 58 (1), 267–288.
Tucker, C.J., Vanpraet, C.L., Sharman, M.J., Van Ittersum, G., 1985. Satellite remote sensing of total herbaceous biomass production in the Senegalese Sahel: 1980–1984. Remote Sens. Environ. 17 (3), 233–249.
USDA National Agricultural Statistics Service (NASS), 2018. Quick stats. Available at: https://quickstats.nass.usda.gov/results/6ED88A30-0BCC-37D0-A6D3-5B0BE7A680CD.
Verma, M., Friedl, M.A., Law, B.E., Bonal, D., Kiely, G., Black, T.A., Wohlfahrt, G., Moors, E.J., Montagnani, L., Marcolla, B., Toscano, P., 2015. Improving the performance of remote sensing models for capturing intra-and inter-annual variations in daily GPP: An analysis using global FLUXNET tower data. Agric. For. Meteorol. 214, 416–429.
Verma, M., Friedl, M.A., Richardson, A.D., Kiely, G., Cescatti, A., Law, B.E., Wohlfahrt, G., Gielen, B., Roupsard, O., Moors, E.J., Toscano, P., 2014. Remote sensing of annual terrestrial gross primary productivity from MODIS: an assessment using the FLUXNET La Thuile data set. Biogeosci. 11 (8), 2185–2200.
Vermote, E., 2015. MOD09A1 MODIS/Terra surface reflectance 8-day L3 global 500m SIN Grid V006 [data set]. NASA EOSDIS Land Process. DAAC. https://doi.org/10.5067/MODIS/MOD09A1.006.
Vermote, E., Wolfe, R., 2015a. MOD09GQ MODIS/Terra surface reflectance daily L2G global 250m SIN grid V006 [data set]. NASA EOSDIS Land Process. DAAC. https://doi.org/10.5067/MODIS/MOD09GQ.006.
Vermote, E., Wolfe, R., 2015b. MYD09GQ MODIS/aqua suface reflectance daily L2G global 250m SIN grid V006 [data set]. NASA EOSDIS Land Process. DAAC. https://doi.org/10.5067/MODIS/MYD09GQ.006.
Veroustraete, F., Sabbe, H., Eerens, H., 2002. Estimation of carbon mass fluxes over Europe using the C-Fix model and Euroflux data. Remote Sens. Environ. 83 (3), 376–399.
Wang, S., Huang, K., Yan, H., Yan, H., Zhou, L., Wang, H., et al., 2015. Improving the light use efficiency model for simulating terrestrial vegetation gross primary production by the inclusion of diffuse radiation across ecosystems in China. Ecol. Complex. 23, 1–13.
Wang, S., Ibrom, A., Bauer-Gottwein, P., Garcia, M., 2018. Incorporating diffuse radiation into a light use efficiency and evapotranspiration model: An 11-year study in a high latitude deciduous forest. Agric. For. Meteorol. 248, 479–493.
Wang, X., Wang, S., Li, X., Chen, B., Wang, J., Huang, M., Rahman, A., 2020a. Modelling rice yield with temperature optima of rice productivity derived from satellite NIRv in tropical monsoon area. Agric. For. Meteorol. 294, 108135.
Wang, S., Zhang, Y., Ju, W., Porcar-Castell, A., Ye, S., Zhang, Z., et al., 2020b. Warmer spring alleviated the impacts of 2018 European summer heatwave and drought on vegetation photosynthesis. Agric. For. Meteorol. 295, 108195.
Virkkala, A.M., Aalto, J., Rogers, B.M., Tagesson, T., Treat, C.C., Natali, S.M., Watts, J.D., Potter, S., Lehtonen, A., Mauritz, M., Schuur, E.A., 2021. Statistical upscaling of ecosystem CO2 fluxes across the terrestrial tundra and boreal domain: Regional patterns and uncertainties. Glob. Chang. Biol. 27 (17), 4040–4059.
Wang, R., Gamon, J.A., Emmerton, C.A., Springer, K.R., Yu, R., Hmimina, G., 2020c. Detecting intra-and inter-annual variability in gross primary productivity of a North American grassland using MODIS MAIAC data. Agric. For. Meteorol. 281, 107859.
Wang, S., Zhang, Y., Ju, W., Qiu, B., Zhang, Z., 2021. Tracking the seasonal and inter-annual variations of global gross primary production during last four decades using satellite near-infrared reflectance data. Sci. Total Environ. 755, 142569.
Wang, H., Yan, S., Ciais, P., Wigneron, J.P., Liu, L., Li, Y., et al., 2022. Exploring complex water stress–gross primary production relationships: Impact of climatic drivers, main effects, and interactive effects. Glob. Chang. Biol. 28 (13), 4110–4123.
Wu, X., Ju, W., Zhou, Y., He, M., Law, B.E., Black, T.A., et al., 2015. Performance of linear and nonlinear two-leaf light use efficiency models at different temporal scales. Remote Sens. 7 (3), 2238–2278.
Wu, X., Xiao, X., Zhang, Y., He, W., Wolf, S., Chen, J., et al., 2018. Spatiotemporal consistency of four gross primary production products and solar-induced chlorophyll fluorescence in response to climate extremes across CONUS in 2012. J. Geophys. Res. Biogeosci. 123 (10), 3140–3161.
Wu, G., Guan, K., Jiang, C., Peng, B., Kimm, H., Chen, M., et al., 2020. Radiance-based NIRv as a proxy for GPP of corn and soybean. Environ. Res. Lett. 15 (3), 034009.
Wu, G., Guan, K., Jiang, C., Kimm, H., Miao, G., Bernacchi, C.J., et al., 2022. Attributing differences of solar-induced chlorophyll fluorescence (SIF)-gross primary production (GPP) relationships between two C4 crops: corn and miscanthus. Agric. For. Meteorol. 323, 109046.
Wutzler, T., Lucas-Moffat, A., Migliavacca, M., Knauer, J., Sickel, K., Šigut, L., et al., 2018. Basic and extensible post-processing of eddy covariance flux data with REddyProc. Biogeosciences 15 (16), 5015–5030.
Xiao, X., Hollinger, D., Aber, J., Goltz, M., Davidson, E.A., Zhang, Q., Moore III, B., 2004a. Satellite-based modeling of gross primary production in an evergreen needleleaf forest. Remote Sens. Environ. 89 (4), 519–534.
Xiao, X., Zhang, Q., Braswell, B., Urbanski, S., Boles, S., Wofsy, S., et al., 2004b. Modeling gross primary production of temperate deciduous broadleaf forest using satellite images and climate data. Remote Sens. Environ. 91 (2), 256–270.
Xiao, J., Chevallier, F., Gomez, C., Guanter, L., Hicke, J.A., Huete, A.R., et al., 2019. Remote sensing of the terrestrial carbon cycle: A review of advances over 50 years. Remote Sens. Environ. 233, 111383.
Yamori, W., Noguchi, K.O., Hikosaka, K., Terashima, I., 2010. Phenotypic plasticity in photosynthetic temperature acclimation among crop species with different cold tolerances. Plant Physiol. 152 (1), 388–399.
Yan, H., Wang, S.Q., Billesbach, D., Oechel, W., Bohrer, G., Meyers, T., et al., 2015. Improved global simulations of gross primary product based on a new definition of water stress factor and a separate treatment of C3 and C4 plants. Ecol. Model. 297, 42–59.
Yang, P., van der Tol, C., 2018. Linking canopy scattering of far-red sun-induced chlorophyll fluorescence with reflectance. Remote Sens. Environ. 209, 456–467.
Yang, X., Tang, J., Mustard, J.F., Lee, J.E., Rossini, M., Joiner, J., et al., 2015. Solar-induced chlorophyll fluorescence that correlates with canopy photosynthesis on diurnal and seasonal scales in a temperate deciduous forest. Geophys. Res. Lett. 42 (8), 2977–2987.
Yang, R., Wang, J., Zeng, N., Sitch, S., Tang, W., McGrath, M.J., et al., 2022. Divergent historical GPP trends among state-of-the-art multi-model simulations and satellite-based products. Earth Syst. Dyn. 13 (2), 833–849.
Yuan, W., Liu, S., Zhou, G., Zhou, G., Tieszen, L.L., Baldocchi, D., et al., 2007. Deriving a light use efficiency model from eddy covariance flux data for predicting daily gross primary production across biomes. Agric. For. Meteorol. 143 (3–4), 189–207.
Yuan, W., Liu, S., Yu, G., Bonnefond, J.M., Chen, J., Davis, K., et al., 2010. Global estimates of evapotranspiration and gross primary production based on MODIS and global meteorology data. Remote Sens. Environ. 114 (7), 1416–1431.
Zeng, Y., Badgley, G., Dechant, B., Ryu, Y., Chen, M., Berry, J.A., 2019. A practical approach for estimating the escape ratio of near-infrared solar-induced chlorophyll fluorescence. Remote Sens. Environ. 232, 111209.
Zhang, L.X., Zhou, D.C., Fan, J.W., Hu, Z.M., 2015. Comparison of four light use efficiency models for estimating terrestrial gross primary production. Ecol. Model. 300, 30–39.
Zhang, Y., Song, C., Sun, G., Band, L.E., McNulty, S., Noormets, A., et al., 2016. Development of a coupled carbon and water model for estimating global gross

primary productivity and evapotranspiration based on eddy flux and remote sensing data. Agric. For. Meteorol. 223, 116–131.
Zhang, Y., Xiao, X., Wu, X., Zhou, S., Zhang, G., Qin, Y., Dong, J., 2017. A global moderate resolution dataset of gross primary production of vegetation for 2000–2016. Sci. Data 4 (1), 1–13.
Zhang, Y., Joiner, J., Alemohammad, S.H., Zhou, S., Gentine, P., 2018. A global spatially contiguous solar-induced fluorescence (CSIF) dataset using neural networks. Biogeosciences 15 (19), 5779–5800.
Zhang, J., Guan, K., Peng, B., Pan, M., Zhou, W., Jiang, C., Kimm, H., Franz, T.E., Grant, R.F., Yang, Y., 2021. Sustainable irrigation based on co-regulation of soil water supply and atmospheric evaporative demand. Nat. Commun. 12 (1), 1–10.
Zhang, J., Xiao, J., Tong, X., Zhang, J., Meng, P., Li, J., et al., 2022. NIRv and SIF better estimate phenology than NDVI and EVI: Effects of spring and autumn phenology on ecosystem production of planted forests. Agric. For. Meteorol. 315, 108819.
Zhao, M., Heinsch, F.A., Nemani, R.R., Running, S.W., 2005. Improvements of the MODIS terrestrial gross and net primary production global data set. Remote Sens. Environ. 95 (2), 164–176.
Zhou, Y., Wu, X., Ju, W., Chen, J.M., Wang, S., Wang, H., et al., 2016. Global parameterization and validation of a two-leaf light use efficiency model for predicting gross primary production across FLUXNET sites. J. Geophys. Res. Biogeosci. 121 (4), 1045–1072.
Zhou, S., Zhang, Y., Williams, A.P., Gentine, P., 2019. Projected increases in intensity, frequency, and terrestrial carbon costs of compound drought and aridity events. Sci. Adv. 5 (1), eaau5740.